CHALMERS
UNIVERSITY OF TECHNOLOGY

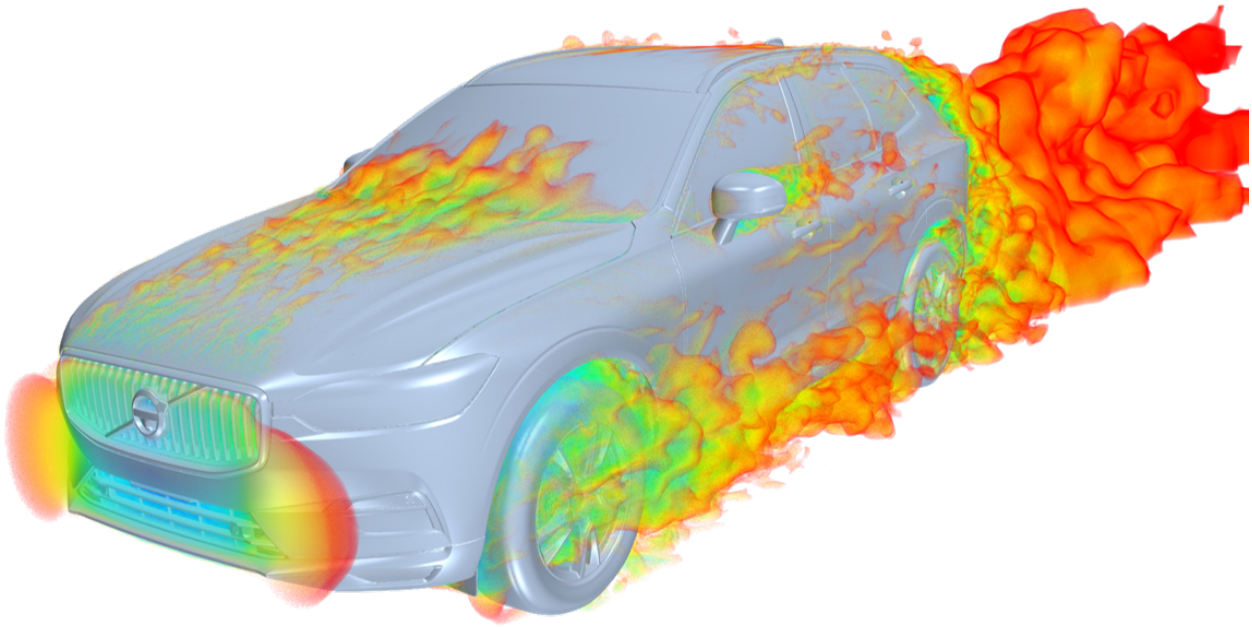

CFD investigation on wheel modelling and car aerodynamics

Master's Thesis in Applied Mechanics

Anandh Ramesh Babu

Department of Mechanics and Maritime Sciences
CHALMERS UNIVERSITY OF TECHNOLOGY
Gothenburg, Sweden 2019

Master's thesis 2019:58

CFD investigation on wheel modelling and car aerodynamics

Anandh Ramesh Babu

CHALMERS
UNIVERSITY OF TECHNOLOGY

Department of Mechanics and Maritime Sciences
Division of Vehicle Engineering and Autonomous Systems
Chalmers University of Technology
Gothenburg, Sweden 2019

CFD investigation on wheel modelling and car aerodynamics
Master's Thesis Report
Anandh Ramesh Babu

Supervisor: Dr. Teddy Hobeika, Aerodynamics Group, Volvo Cars
Examiner: Prof. Simone Sebben, Division of Vehicle Engineering and Autonomous Systems, Chalmers University of Technology

Master's Thesis 2019:58
Department of Mechanics and Maritime Sciences
Division of Vehicle Engineering and Autonomous System
Chalmers University of Technology
SE-412 96 Gothenburg
Telephone +46 31 772 1000

Cover: Resampled volume used to capture regions of low instantaneous velocities around the car.

Typeset in LaTeX
Printed by Chalmers Reproservice
Gothenburg, Sweden 2019

CFD investigation on wheel modelling and car aerodynamics
Master's Thesis
Anandh Ramesh Babu
Department of Mechanics and Maritime Sciences
Chalmers University of Technology

Abstract

It has been estimated that approximately 25% of the drag of a passenger vehicle is due to the wheels and wheel housings. So studying the flow patterns around them have been of great importance for several years. Traditionally, wind tunnel experiments have been used to study the aerodynamic performance of vehicles but with growing computational resources, CFD investigations have proven to be vital, especially in the initial stages of development. With growing regulations on vehicle performances, it is of paramount importance to be able to accurately simulate the flow around wheels. The work included two studies: simulations of a rotating cylinder to represent a simplified wheel geometry and simulations of a full scale car.

In the first study, the Rotating Wall(RW) and Sliding Mesh(SM) methods were investigated on a cylinder and it was found that the case was extremely mesh and timestep dependent. To obtain comparable results, very fine mesh and timestep had to be employed which were computationally expensive. A parametric study was performed on the SM case to understand the mesh, geometry and timestep dependency. Investigations were done to see if pseudo-parallelization of mesh updating in SM method could speed up the simulations. About 35% reduction in total time and 68% reduction in mesh updating time was noted.

In the second study, aerodynamic analysis was performed on the car and wheels. Moving Reference Frame(MRF) and SM wheel modelling approaches were investigated and their differences were analyzed. Investigations on how blanking of rims affect the aerodynamic performance of a car was performed. It was noted that blanking reduced the drag by about 29 C_dA counts and increased downforce by 21 C_lA counts. An investigation on whether performing simulations with a timestep of 2.5e-4s on the mesh was done by comparing the results to a finer timestep of 1e-4s. It was found that the 2.5e-4s yields acceptable results. Finally, pseudo-parallelization of the interface updating was tested on the car by splitting the wheel interface into three interfaces. About 21% reduction in updating time and 5% reduction in total time was observed using this method. It was inferred that the method can be used for speeding up SM simulation and it can be further improved by creating more interfaces and evenly distributing the number of cells on each interface.

Keywords: Car aerodynamics, CFD, wheel modelling, SM optimizing, wheel blanking, pseudo-parallelization of SM.

Acknowledgements

Firstly, I would like to express my sincere gratitude to my supervisor at Volvo Cars, Dr. Teddy Hobeika, for his constant support and motivation, guiding me in the right direction during the course of this project. His insightful recommendations in the project has proven to be extremely helpful to me. I would also like to thank him for teaching me a great deal about aerodynamics of passenger vehicles and CFD modelling.

I would like to thank my examiner, Prof. Simone Sebben, for her valuable advice and for all the help when needed.

Another sincere thanks to everyone at Volvo Cars and the aerodynamics department, for giving me the opportunity to work in such an encouraging environment and your valuable lessons in table tennis.

And finally, a big thanks to my parents and all my friends in Gothenburg and back in India, who have always believed and encouraged me all these years. I am sure that all the support and unconditional love you have given me, is the reason I am an engineer today.

Anandh Ramesh Babu, Gothenburg, June 2019

Contents

List of Figures

List of Tables

1
Introduction

1.1 Environmental impact of Vehicle Aerodynamics

Over the last few decades, concerns pertaining to climate change and global warming have increased. Climate scientists predict adverse impacts on the environment over the next decade if industrialization continues at the current rate. This rise in temperature could have devastating effects on the planet ranging from melting of polar ice caps, rise in sea level, erratic rainfall and so on. The increase in CO_2 levels in the atmosphere is a key green house ingredient for this issue.

The transport industry is a major producer of CO_2 gas. Combustion of various types of fuels releases numerous harmful gases and even particulate matter in some cases. Sometimes, it is difficult to convert them into less harmful substances using filters and catalysts. So, authorities had to intervene and introduce regulations to control the amount of emissions that vehicles produce. The European Union Council aims to restrict the CO_2 emissions to about 95g/km by 2020 [4]. Since then, energy efficiency has been a priority. The forces making up for the driving resistance are summarized in Eq. 1.1 which consists of aerodynamic drag, inertial force, rolling and climbing resistance.

$$F_{drive} = \frac{1}{2}\rho U_\infty^2 C_D A + ma + mgf_F cos\alpha + mgsin\alpha \tag{1.1}$$

where ρ is the density of air, U_∞ is the freestream velocity, C_D is the coefficient of drag, A is the reference area, m is the mass of the vehicle, a is the acceleration of the vehicle, f_F is the frictional coefficient, g is the acceleration due to gravity and α is angle at which the vehicle moves relative the horizontal. Minimizing the forces is key in reducing energy consumption. Out of the four terms, only aerodynamic drag does not contain mass of the object and depends on size, shape and velocity. C_D depends on the shape, size of the object and is a function of the square of velocity. Hence reducing this term can result in considerable change to the effective driving resistance [2].

Standardizing driving cycles to compare the fuel consumption of different vehicles on common basis forms the foundation for determining the official fuel consumption. With the currently used New European Driving Cycle (NEDC) cycle, the gap between cycle consumption and real world consumption has been increas-

ing. So, Worldwide harmonized Light vehicles Test Procedures has been implemented. WLTP has an average impact speed of 46km/h as compared to 34km/h on NEDC[3][5]. With this new cycle, aerodynamics has been given more importance given the drag is a function of the square of velocity.

1.2 Background

Trends in Computer Aided Engineering(CAE) increasingly impact a vehicle's development and plays an important role in today's automotive sector. Traditionally, wind tunnel experiments had been used to analyze flow patterns and improve car aerodynamics. This proved to be expensive and time-consuming especially in the early phases. With the development of modern CFD tools and turbulence models, initial testing and analysis has become more feasible. Even complex modeling such as wheel rotations is now more accurate and realistic with the modern tools.

Although modeling wheel rotation is relatively new, wheel aerodynamics has been carried out for over 4 decades. Although the wheel is split into tyre and rim, the aerodynamic effects of each cannot be separated easily and their effects interact with each other continuously. Fackery and Harvey [7] were among the first ones to investigate isolated, rotating wheel in contact with a moving ground experimentally. It was shown that grooves reduced the pressure peak at the contact patch by equalizing the pressure in front of and behind it. Cogotti[8] and Merceker[9] described vortex systems behind isolated wheels. Elofsson and Bannister[10] performed tests on different vehicle shapes with wheel rotation and they concluded that local decrease in drag was noted from front wheel rotation but that did not necessarily reduce the global drag. The largest effect arose from the rear wheel rotation and its influence on the base wake. From a computational study performed by Landström et al [11] on a saloon type car, a radial cover of 30mm showed a drag reduction of 10 C_d counts. Similarly, from a study by Qiu et al. [12] , several rim configurations were tested and a fully blanked wheel gave a drag reduction of 17 C_d counts, while a similar configuration from Landström showed 7 counts. Hobeika et al. [1][13][14] investigated the different methods of modeling rotation of tyre and wheel geometries computationally and the effects of wheel geometry on the flow stream. In this study, it was noted that, rain grooves on tyres reduced the drag of a passenger car as compared to slick tyres. Sofie et al. [15] investigated the effects of wheel blanking of varied degrees and concluded that blanking decreases drag. The study also compared the accuracy of CFD results with experimental data for difference sets of rim geometry.

CFD simulations produce numerical solutions of real scenarios relying on assumptions and mathematical models. With proper corrections and relaxations on the equations, CFD results can be correlated to experiments. Blacha et al. [16] described an extensive study on using CFD for the aerodynamic development of Audi Q5 and an account of how turbulence models work for aerodynamic simulations. Bastian et al. [17] investigated Lattice Boltzmann approach to model rotation of an

isolated wheel. They found that the contact patch separation was highly sensitive to load variations while modeling tyre deformations. They also suggested coupled FEA-CFD solvers to model tyre deformation in CFD simulations. Profir M. M [18] investigated automated meshing and remeshing techniques to model motion in CFD applications using java scripts. But the above mentioned methods to model contact patches are computationally expensive.

Previous CFD investigations have been performed to model wheel rotation. The available methods are Rotating Wall, Moving Reference Frame and Sliding Mesh methods. It was found that using RW method on wheels resulted in inaccurate prediction of rim velocities. MRF and SM methods are the most commonly used methods to model wheels. SM method is computationally expensive but it accounts for rotation of wheels by physically moving the mesh. MRF method accounts for rotation by modifying the reference frame in the governing equations. It was observed that MRF method produced unphysical flow field when applied on rotating cylinders. Modeling tyre rotation due to contact patch deformation is difficult using SM. Hence the common practice for modeling wheels is, to use RW for the tyres(valid only for slick or rain grooves; lateral grooves on tyres produce unphysical velocity field) and MRF or SM for the rims. Lateral grooves can be modelled using MRFg which is a combination of MRF and RW. A detailed account on this can be found in [1].

The SM method is computationally expensive in all CFD commercial tools. In the CFD tool by Siemens, Star-CCM+, SM approach, which is called Rigid Body Motion in the software, is no different. The mesh updating step is a serial operation in this software. At the end of each timestep, the solver needs to stop after each timestep, update the mesh and then restart the solver for the next timestep. It has been found that, the speed of interface updating is highly dependent on the number of intersecting faces between the stationary and rotating regions. So, by splitting the interface into multiple boundary interfaces, the load on the CPU is effectively reduced and this process of updating can be made more efficient while still being a serial process. Thus, this approach can be termed as pseudo-parallelization.

1.3 Project Objectives

The objectives of this project are listed below:

- Study rotation modelling(RW and SM) on a rotating cylinder.
- Analyze flow field around a car and wheels.
- Analyze the differences between MRF and SM methods for wheel modelling.
- Study the effects of blanking a rim on the aerodynamic performance of a car.
- Investigate pseudo-parallelization on the cylinder and car cases.

2
Theory

This chapter explains the theoretical background required to understand the different concepts and methods used in the project. Firstly, the basics of fluid dynamics starting from the concepts of continuum are explained, followed by CFD and its various formulations and governing equations. Then concepts specific to a car aerodynamics are explained. Finally, the various methods used for rotational wheel modeling of a car.

2.1 Fluid Dynamics

Fluid dynamics deals with the study of fluid flow. A fluid can be liquid, gas or a combination of both in some cases. Matter is made up of discrete molecules and the density with which they are packed defines its state. Fluid state has particles with relatively low density as compared to solids. The particles in fluids are in a state of random motion always colliding with each other. In general for engineering problems, matter is not studied in such microscopic scales whereas they are visualized and studied in a more macroscopic level known as continuum.

In continuum, it is noted that the length and time scales of matter are larger than the microscopic scales. The solutions to a fluid dynamics problem in continuum scales typically represents the flow in terms of properties such as pressure, density, flow velocity as functions of space and time. [22]

This framework of definition is given by the conservation laws- conservation of mass, momentum and energy. The Navier-Stoke's equations are obtained by formulating the above mentioned principles to characterize fluid flow. These equations are applied in fluid dynamics problems, either in full or a simplified form and used in various applications.

2.1.1 Governing Equations

The Navier-Stoke's equation is a set of partial differential equations with basically consists of the continuity equation and momentum conservation equation as stated in Eq. 2.1 and Eq. 2.2.

The continuity equation or the mass conservation equation states that the rate of increase of mass in the system is equal to the net rate of the mass flow into the

system.

$$\frac{\partial \rho}{\partial t} + \frac{\partial \rho v_i}{\partial x_i} = 0 \tag{2.1}$$

The first term in the Eq. 2.1 is the unsteady term which accounts for the change in density of the fluid with time. The second term is the convection term which accounts for the net change in mass flow rate across the boundaries. This equation states that mass entering the system should be equation to the mass exiting.

The momentum conservation equation states that the rate of change of momentum is equal to the net forces acting on the fluid.

$$\rho \frac{dv_i}{dt} = -\frac{\partial P}{\partial x_i} + \frac{\partial \tau_{ij}}{\partial x_j} + \rho f_i \tag{2.2}$$

The first term in the Eq. 2.2 is a total differential term of velocity. This means that terms is,

$$\frac{dv_i}{dt} = \frac{\partial v_i}{\partial t} + \frac{\partial v_i v_j}{\partial x_j}$$

The first term in the right hand side of Eq. 2.2 is the negative gradient of pressure which acts the source term. The second term is the gradient of stresses(τ_{ij}) acting on the fluid and the last term signifies the body forces on the fluid. The viscous stress tensor is defined as,

$$\tau_{ij} = 2\mu S_{ij} - 2\mu S_{kk}\delta_{ij} \tag{2.3}$$

$$S_{ij} = \frac{1}{2}\left(\frac{\partial v_i}{\partial x_j} + \frac{\partial v_j}{\partial x_i}\right) \tag{2.4}$$

The conservation of energy equation is derived from the first law of thermodynamics, which states that the rate of change of energy of a fluid is equal to the sum of rate of heat addition to the fluid and rate of work done. The energy conservation equation is stated in Eq. 2.5.

$$\frac{\partial \rho E}{\partial t} + \frac{\partial v_j E}{\partial x_j} = -\rho q + \frac{\partial}{\partial x_j}\left(k\frac{\partial T}{\partial x_j}\right) - \frac{\partial v_j p}{\partial x_j} + \frac{v_i \tau_{ij}}{\partial x_j} + \rho f_i v_i \tag{2.5}$$

Where E is the total energy of a moving fluid element and E is defined as,

$$E = e + \frac{1}{2}v^2$$

where e is the internal energy per unit mass and $\frac{v^2}{2}$ is the kinetic energy per unit mass and p is the pressure which is given by the ideal gas law $p = \rho RT$

Unless the flow is compressible or cases where heat transfer is involved, the energy equation is not considered in the solution. So, for aerodynamics of automobiles, where flow is incompressible and no heat transfer is involved, only the continuity equation and momentum equation are considered.

2.2 Computational Fluid Dynamics

Solution of the Navier-Stokes equations are problem specific and analytic solution to the problem is extremely difficult to perform. So, usually numerical methods are applied. With growing computational power, CFD has gained significant importance over the past few decades.

Using numerical methods, the governing equations of fluid flow are discretized in space and time based on different discretization schemes. By applying boundary conditions to the discretized equations, the solutions are obtained based on the given accepted level of accuracy. Since the continuum is split into discrete segments in space and time for numerics, the accuracy is greatly dependant on their sizes. For accuracy, it is recommended to have finely discretized mesh and time.

The fluctuations in flow parameters present in turbulent flows, occur locally in the flow. These fluctuations define the flow energy and they need to be studied closely.

2.2.1 Turbulence

Almost all flows around us are turbulent in nature, from combustion in engines and turbines to flow around automobiles and airplanes. Turbulence is governed by eddies, which are swirling irregular scale of different sizes. They cause abrupt changes in flow velocity locally.

The turbulent scales are important in understanding turbulence. The scales are differentiated based on size into large scales, intermediate scales and dissipative scales. The large scales of the order of the flow geometry and flow velocity. These scales extract kinetic energy from the mean flow. Part of the kinetic energy is transferred slightly smaller eddies by collision with other larger eddies. Through cascade process, the energy is transferred to the smallest scales (Kolmogorov scales) where it is dissipated.

The flow in turbulent regime is chaotic and irregular and yet the Navier-Stoke's equations govern it. The main advantage of this is that every detail of the turbulent velocity field, from the largest to the smallest scales is described. Thus an extensive amount of information is described by the Navier-Stoke's equation and as a result, the direct approach of solving them, Direct Numerical Solution (DNS), is available but impractical. So, turbulence models are used which are statistical in nature which depend on the mean velocity field to represent the turbulent flows.

The most common models are RANS : $k - \epsilon$, $k - \omega$, LES and DES models. A few turbulent models are described below.[23]

2.2.2 RANS models

Reynolds Averaged Navier Stoke's equation is a time averaged Navier-Stokes equation. A turbulent flow field can be decomposed into a mean and a fluctuating part.

$$u_i = \bar{u_i} + u_i' \tag{2.6}$$

Where $\bar{u_i}$ is the mean part and u_i' is the fluctuating part. Each term in the continuity and momentum equation can be decomposed in such fashion. The resulting equation when Reynolds averaging these equation is called Reynolds Averaged Navier-Stokes equation.

$$\frac{\partial \bar{u_i}}{\partial x_i} = 0 \tag{2.7}$$

$$\rho \frac{\partial \bar{u_i}\bar{u_j}}{\partial x_j} = -\frac{\partial p}{\partial x_i} + \frac{\partial}{\partial x_j}\left(\mu \frac{\partial \bar{u_i}}{\partial x_j} - \rho \bar{u_i'u_j'}\right) \tag{2.8}$$

Where $\rho u_i' u_j'$ is the Reynolds stress tensor which is a unknown. This term is a consequence of averaging. The RANS based models aim to model this term to close the equation.

Unsteady RANS models have been developed which retains the same form as the RANS equation stated in Eq. 2.8 along with an unsteady velocity term in the left hand side which accounts for the rate of change of velocity.

In the problem at hand, $k-\omega$ turbulence model is used and so it is briefly explained below.

2.2.2.1 $k-\omega$ Turbulence Model

The $k-\omega$ model is one of the most popular models used in CFD simulations. It is a two equation eddy viscosity model that solves the RANS equations in addition to two partial differential equations for k, the kinetic energy as in Eq. 2.9 and ω, specific rate of dissipation as in Eq. 2.10.

$$\frac{\partial \rho k}{\partial t} + \frac{\partial (\rho u_j k)}{\partial x_j} = \frac{\partial}{\partial x_j}\left(\left(\mu_t + \sigma_k \frac{\rho k}{\omega}\right)\frac{\partial k}{\partial x_j}\right) + P_k - \beta^* \rho \omega k \tag{2.9}$$

$$\frac{\partial \rho \omega}{\partial t} + \frac{\partial (\rho u_j \omega)}{\partial x_j} = \frac{\partial}{\partial x_j}\left(\left(\mu_t + \sigma_w \frac{\rho k}{\omega}\right)\frac{\partial \omega}{\partial x_j}\right) + \frac{\gamma \omega}{k} P_k - \beta^* \rho \omega^2 \tag{2.10}$$

Where μ_t is eddy viscosity which is given by, $\mu_t = \rho k/\omega$ and β^* is a constant is usually equal to 0.09.

$$P_k = \tau_{ij} \frac{\partial u_i}{\partial x_j} \tag{2.11}$$

$$\tau_{ij} = \mu_t \left(2S_{ij} - \frac{2}{3}\frac{\partial u_k}{x_k}\right) - \frac{2}{3}\rho k \delta_{ij} \tag{2.12}$$

$$S_{ij} = \frac{1}{2}\left(\frac{\partial u_i}{\partial x_j} + \frac{\partial u_j}{\partial x_i}\right) \tag{2.13}$$

The Eq. 2.9 and Eq. 2.10 have the same structure. The first term is the unsteady term which defines the rate of change of the quantity. The second term is the convection of the quantity. The third term is turbulent diffusion of the the quantity. The fourth term defines the production term and finally the rate of dissipation of the quantity.

2.2.3 LES model

The basic principle of Large Eddy Simulation (LES) is to resolve the large grid scales (GS) and model the small subgrid scales (SGS) of the turbulence. In LES, the equations are volume averaged and since it is not averaged in time, the volume averaged equations are functions of both space and time. Hence, the LES model gives a transient solution in contrary to a RANS simulation. Since a part of the turbulent scales are resolved and a transient solution is required, LES is much more computationally expensive than a RANS simulation, but also more accurate since less turbulence is modeled. The LES model requires a very fine mesh, especially in the boundary layer, in order to give a good solution.

Due to the volume averaging, the turbulent eddies are filtered so that the small scales are not solved for. The quantities are decomposed into a filtered part and a subgrid part as

$$\phi = \bar{\phi} + \phi' \tag{2.14}$$

The equations for the filtered variables have the same form as Navier-Stokes equations,

$$\frac{\partial v_i}{\partial t} + \frac{\partial}{\partial x_j}(\bar{v_i}\bar{v_j}) = -\frac{1}{\rho}\frac{\partial \bar{p}}{\partial x_i} + \nu\frac{\partial^2 \bar{v_i}}{\partial x_j \partial_j} - \frac{\partial \tau_{ij}}{\partial x_j} \tag{2.15}$$

$$\frac{\partial \bar{v_i}}{\partial x_i} = 0 \tag{2.16}$$

where $\bar{v_i}$ is the filtered velocity, $\bar{p}$ is the filtered pressure, ρ is the density, ν is kinematic viscosity and τ_{ij} is subgrid stress tensor which is given by, $\tau_{ij} = v_i\bar{v}_j - \bar{v_i}\bar{v_j}$. The subgrid stress tensor term needs to be modeled. Different LES models such as Smagorinsky model, dynamic model and mixing length model aim in closing the equation by modeling the subgrid stresses.

2.2.4 DES models

Detached Eddy Simulation (DES) is a combination of LES and URANS which is commonly referred to as hybrid RANS-LES. URANS is used inside the boundary layer, while LES is used to resolve the detached eddies outside of the boundary layer. Thus DES uses the advantage of the accuracy of LES, while not requiring an extremely fine mesh inside the boundary layer due to the usage of URANS. The transition between the equations used for URANS and LES takes place through reducing the turbulent viscosity. The length scale in DES model is dependant on the grid size and so the creating an appropriate mesh is crucial for the switch between URANS and LES models. In order to overcome this, DDES model was proposed

which protects the boundary layer from LES by preventing early switches from RANS to LES. This was achieved by introducing blending and shielding functions. The shielding functions are based on wall distance and eddy-viscosity. DES and DDES are explained in detail in [22].

2.2.4.1 IDDES model

With suitable formulations in the shielding and blending functions, DDES can be formulated in Wall Modelled LES (WMLES) mode. The length scale in this model is a piece wise functions incorporating wall distance dependency and local cell size. The modified sub-grid length scale accounts for anisotropic effects which results in in significantly varying length scales that helps the flow destabilize. The DDES part is designed to activate in flows without turbulent inflow and in cases where grid is unlikely to resolve the dominant energy carrying eddies while the WMLES part is activated when the unsteady turbulent inflow is provided and when the grid can sufficiently resolve. A more detailed account on IDDES can be found in [21]. In this work, the IDDES model has been used to simulate the cylinder and complete car cases.

2.3 Aerodynamics

Aerodynamics is the study of how fluids interact with moving bodies. Aerodynamics is primarily concerned with the forces and moments caused by air passing over and around solid bodies. These forces, and moments greatly affect the performance and handling of the vehicle, and are commonly decomposed into three rotational and three translational terms. They are represented in Fig. 2.1. The two fundamental forces act on a moving vehicle. The first one is drag, which acts along the direction that resists the desired vehicle motion. Drag can be divided into pressure drag and skin friction drag where the former is the most dominant one. The second force is lift which acts in the direction perpendicular to the direction of vehicle motion. Lift is generated in the vehicle due to the pressure difference between the roof and the underbody of the car. Drag affects the vehicle's performance characteristics while lift affects the directional stability.
In general, lift and drag are non-dimensionalized so that these value represent drag and lift for a particular shape and they can be used for performance comparisons with other shapes. The formulae for computing the C_d and C_l are given below:

$$C_d = \frac{2F_d}{\rho U^2 A_f} \tag{2.17}$$

$$C_l = \frac{2F_l}{\rho U^2 A_f} \tag{2.18}$$

where F_d and F_l are drag and lift forces respectively, ρ is the density of air, U is the velocity of the vehicle and A_f represents the frontal area of the vehicle.

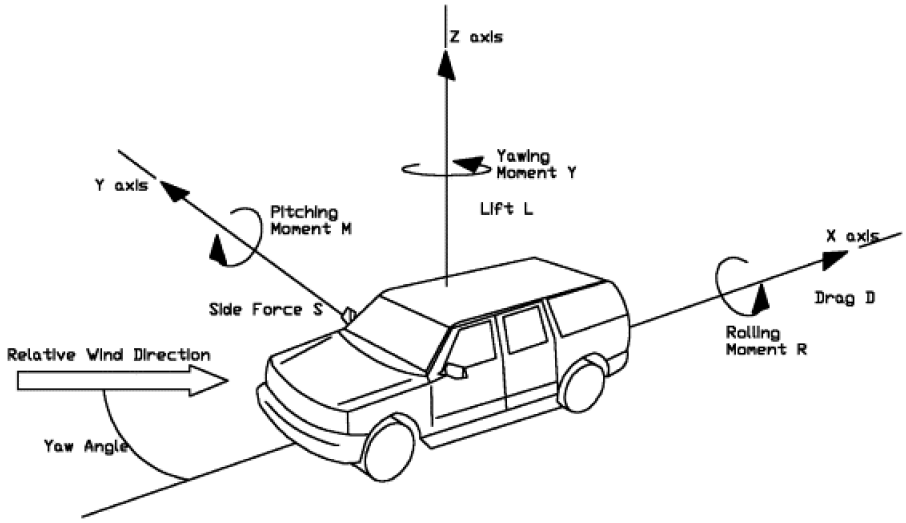

Figure 2.1: Aerodynamic forces and moments acting on the car

2.4 Rotation Modeling

The angular velocity of the wheels can be modelled in many ways with each having certain advantages and disadvantages. And so the method to choose is problem specific. There are three commonly used methods: Rotating Wall method, Moving Reference Frame method and Sliding Mesh method[14][24]. Traditionally MRF method has been used for rim and spokes and RW condition on the tyre. But SM method is also used instead of MRF in some cases. Hybrid methods such as MRFg have been proposed for tyre modelling[1].

2.4.1 Rotating Wall boundary condition

The Rotating wall approach is possibly the simplest way of modelling rotation. In this method, the rotational option allows the user to specify a rotational velocity about a specified axis on a wall boundary. The velocity is applied tangentially to each cell on the boundary. Hence, if the velocity vector is not on the same plane as the cell surface, it is projected thereby losing its normal component. Hence, RW method is not feasible when the velocity vector is normal to the cell surface like in the case of rim spokes and lateral grooves.

2.4.2 Multiple Reference Frame

The MRF approach is implemented by prescribing the fluid cells to a moving frame of reference, in this case, rotation. This allows it to apply a surface velocity normal to the surface and hence produce a desired surface velocity in the region. The user determines a number of regions with defined interfaces between them and in each region, different rotational speeds can be defined. For the absolute velocity formulation, the governing equations of fluid flow for a moving frame is written in Star-CCM+ user guide[19] as follows,

$$\nabla \cdot (\vec{u_p} \times \vec{u_0}) + \vec{\omega_p} \times \vec{u_0} = -\nabla(p/\rho) + \nu \nabla \cdot \nabla \vec{u_0} \tag{2.19}$$

$$\nabla \cdot \vec{u_0} = 0 \tag{2.20}$$

where, u_p is the velocity relative to the moving reference frame, u_0 is the absolute velocity, w_p is the angular velocity of the rotating frame, p is the fluid pressure and ρ is density of the fluid. It also generates centrifugal accelerations and Coriolis effects in the fluid.

If the flow field in an empty MRF region is uniform, then $\nabla.\vec{u_0} = 0$. Then Eq. 2.19 reduces to

$$\nabla p = -\rho(\vec{\omega_p} \times \vec{u_0}) \tag{2.21}$$

Hence, whenever $\vec{\omega_p} \times \vec{u_0} \neq 0$, a pressure gradient is introduced. The pressure gradient becomes zero when the flow is along the axis of rotation. However for wheels, the flow is more complex and the axis of rotation is orthogonal to the flow.

The MRF approach has a number of limitations. The interfaces defined by the user affects the outcome. Additionally for a geometry that is not axisymmetric, the positioning the model during the simulation can have significant effects on the results. This means, two simulations of same CAD geometries can give different results if the position of the spokes is different.

2.4.3 Sliding Mesh method

The Sliding Mesh approach is implemented by physically moving the mesh each time step. This means the simulation is inherently unsteady. The connection between the sliding and stationary region, the interface, needs to be updated every time step. This motion, allows SM to take into account the different positions of the rotating/-moving object. This would be the most realistic way of modelling rotating rigid geometry. However, it would typically result in significant increase in simulation time to update the mesh after each timestep.

The generic transport equation for dynamics meshes is given as,

$$\frac{d}{dt}\int_V \rho\phi dV + \int_{\partial V} \rho\phi(\vec{u} - \vec{u_g}) \cdot d\vec{A} = \int_{\partial V} \Gamma \nabla\phi \cdot d\vec{A} + \int_V S_\phi dV \tag{2.22}$$

Where,
rho is the fluid density,
$\vec{u}$ is the flow velocity,
$\vec{u_g}$ is the mesh velocity of the moving mesh,
Γ is the diffusion coefficient,
S_{phi} is the source term of ϕ,
∂V is used to represent the boundary of the control volume V.

3
Methodology

In this chapter, the different cases and their setup in Star-CCM+ are explained. The project was split into two studies, where the first study comprises of a simple model involving a cylinder is used to verify RW and SM methods. Then a parametric study on the mesh and time step for the sliding mesh was performed. Finally, by splitting the interface between the stationary and moving region of the SM simulation, potential speedup in the mesh updating step was investigated, thereby reducing the time taken per time step. The second part of the project comprised of testing different wheel modelling approaches on a car - Volvo XC60. Additionally open and closed rims were evaluated, time step dependency on the whole car was examined and finally it was investigated if splitting the interface resulted in a speed up of updating time for a car.

3.1 Cylinder Simulations

The objective of the cylinder simulations was that the cylinder represents a simplified model of a wheel without rims and tyre profiles. The objective of the study was to comprehend how rotation modelling techniques worked.
Fig. 3.1 represents the setup used in this section. The domain is a box of dimensions $25m \times 16m \times 0.1m$. A cylinder of radius 0.3m is placed at 10 m from the inlet.

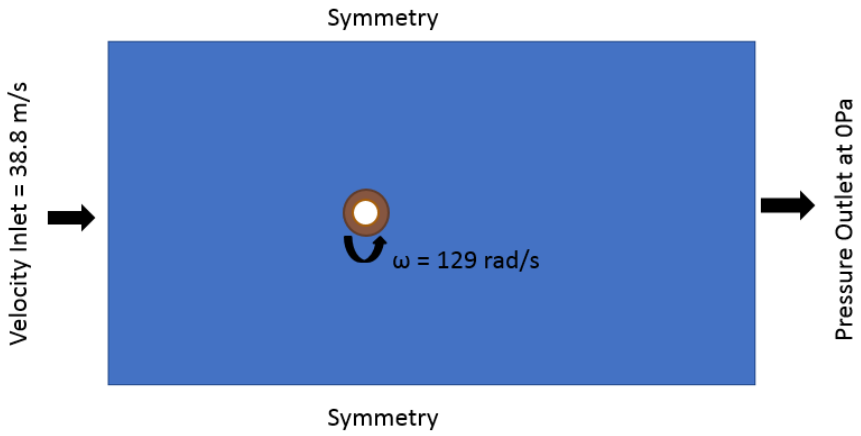

Figure 3.1: Geometry description of the cylinder simulations

The boundary conditions used in the simulations are stated in Table 3.1.

Boundary	Setting
Inlet	Velocity Inlet: 38.89m/s
Outlet	Pressure outlet: 0Pa
Front, Back, top and bottom	Symmetry
Wall	wall (RW includes a tangential velocity specification)

Table 3.1: Boundary conditions for cylinder simulations

The sliding mesh simulation needs a separate region where the mesh physically moves each time step. As seen Fig. 3.2, the grey region represents the rotating region and the blue region represents the stationary air domain. The interface is located at a radius 0.315m from the centre. To maintain consistency in the mesh while comparing RW and SM methods, the same mesh was used.

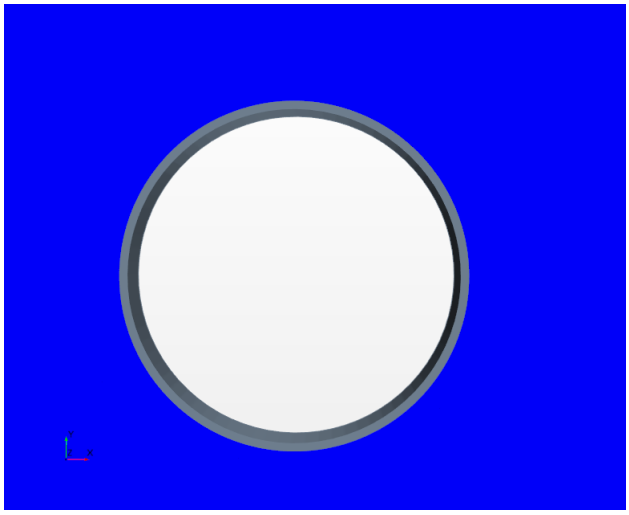

Figure 3.2: Segregation of regions: Grey region represents the rotating region and blue region represents the stationary air domain

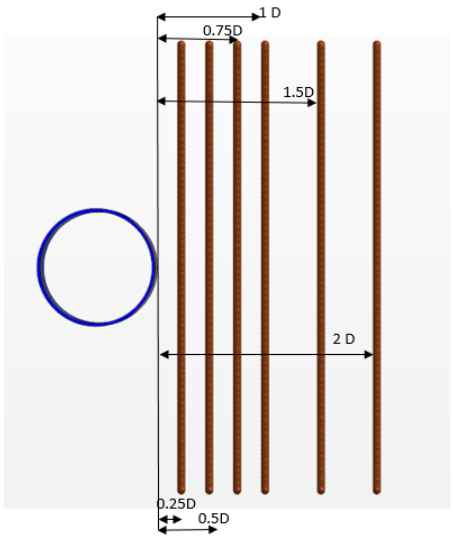

Figure 3.3: line probes

Various reports and monitors of drag, lift and moment in the rotating domain and reports for their time averaged value were set up. The mean of velocity is also calculated and plotted along line probes which are shown in Fig. 3.3.
The line probes are of length 4D placed symmetrically about the X-axis and at distances 0.25D, 0.5D, 0.75D, 1D, 1.5D and 2D from the surface of the cylinder, where D is the diameter of the cylinder.
In the first study, the RW and SM methods were verified for this case. Physically, both the methods are the same. In the RW method, a tangential velocity is prescribed at the cylinder wall by giving a rotational rate and axis of rotation while in SM method, the entire region rotates about the specified axis of rotation at the specified rotational rate.
By taking into account the CFL criterion and the frequency of vortex shedding, the mesh was refined in stages. Finally, a reasonably refined mesh was obtained and it is shown in Fig. 3.4 and Fig.3.5.

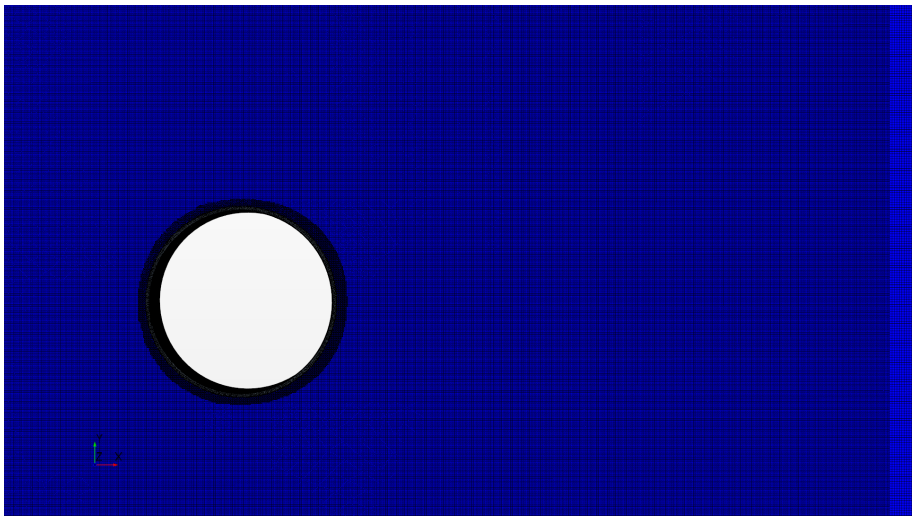

Figure 3.4: Mesh around the cylinder and interface

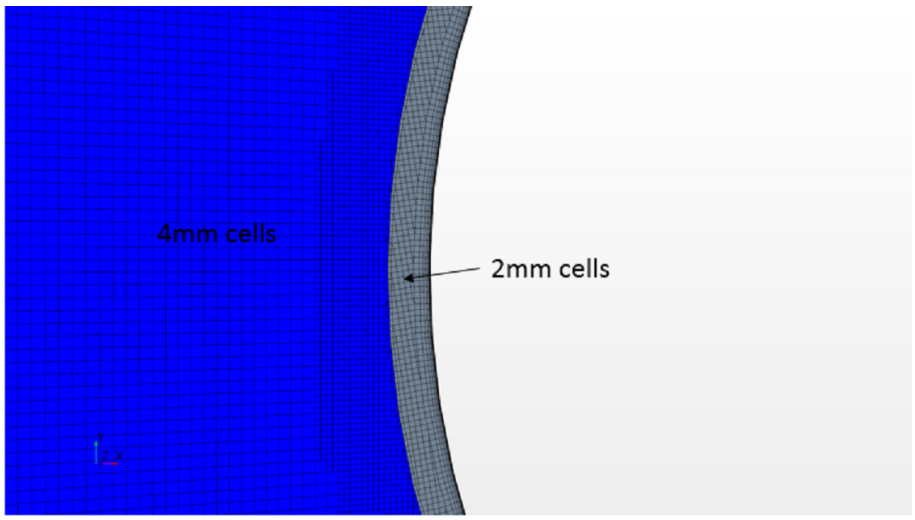

Figure 3.5: Mesh around the cylinder and interface

The cell size was set to 2mm at the cylinder wall and interface. A volume cell refinement was set around the cylinder with a cell size 4mm as shown in Fig. 3.4. The first cell height from the wall was set at 1e-5m to obtain a y+<1 at the wall. Fourteen prism layer were built with a growth ratio of approximately 1.5 which resulted in a total height of 6mm.
The simulation was performed in two stages: first, a steady state SST $k-\omega$ model was used with wall rotation boundary condition on the cylinder wall with a rotational rate of 129.6 rad/s for 1500 iterations. Second, the unsteady IDDES solver was run on RW or SM methods with a time step of 1e-5s and 6 inner iterations for a total physical time of 4s.
The results from the study comparing the two methods are presented in section (4.1.2).
Next, a parametric mesh and time step study was performed on the SM case. The objective of this study was to see how dependent the case was to mesh and time step changes. The parameters tested are given in Table 3.2.

Parameters	**Settings used**
Time average study	4s, 5s
Time step dependency	2.5e-4s, 1e-4s, 1e-5s
Cell size dependency at the wall	2mm, 4mm
Size of the sliding domain	0.315m, 0.36m
Solver	Segregated, Coupled
y+ dependency (first cell height)	1e-4m, 1e-5m

Table 3.2: Parametric study

The simulation performed in the first case, was considered as the ideal or the base case and the solution (forces, moment and mean velocity on the line probes) obtained by varying each of parameter was compared to the solution of the base case.
Finally, the pseudo-parallelization of interface updating was tested where the interface between the rotating region and the domain was split into two, three, four and eight faces. The geometries were modelled using ANSA as shown in Fig. 3.6. The boundaries were interfaced using boundary mode. So, the interfaces branch in simulation tree of Star-CCM+ has a number of interfaces. Reports of elapsed time per time step and elapsed time per iteration and their means were used to analyze if this method could speed up the simulation.

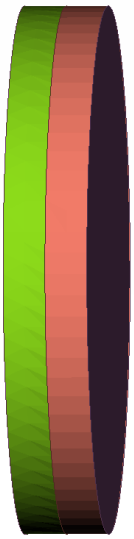

(a) Two interfaces

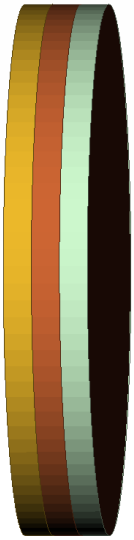

(b) Three interfaces

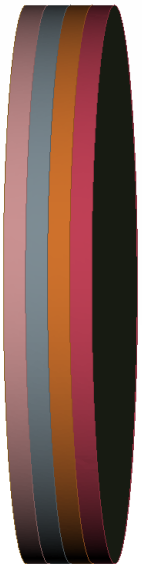

(c) Four interfaces

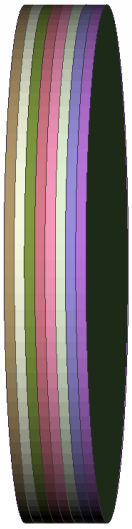

(d) Eight interfaces

Figure 3.6: Geometries of cylinder split into 2, 3, 4 and 8 faces

3.2 Car Simulations

The second part of the project was to perform CFD investigation on the car and wheels. The car used in this case was a Volvo XC60. The domain used in this case is a $70m \times 40m \times 30m$. The existing CAD models of the car with the complete setup was provided by Volvo. The preparations for this study was done in ANSA v.18. The changes were predominantly in the wheel geometry, modeling approach and the sliding mesh region. The complete car geometry is shown in Fig. 3.7.

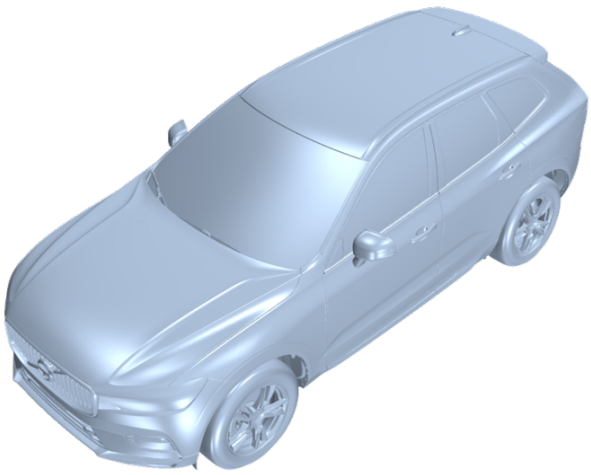

Figure 3.7: Volvo XC60 geometry

The Fig. 3.8 shows the domain with the boundaries, inlet, outlet and ground which are modelled as velocity inlet, pressure outlet and moving wall boundary conditions respectively. By modeling the wall with moving wall boundary condition, development of boundary layer on the wall is prevented. The other surfaces that enclose the domain are modelled as symmetry boundary condition. The surfaces of the car are also modelled as wall. The boundary conditions are given in table 3.3.

Boundary	**Setting**	**Value**
Inlet	Velocity Inlet	140 kmph
Outlet	Pressure Outlet	0 Pa
Ground	Moving wall	140 kmph
Side and top faces of the domain	Symmetry	-
Car surface	Wall	-

Table 3.3: Boundary conditions on the domain

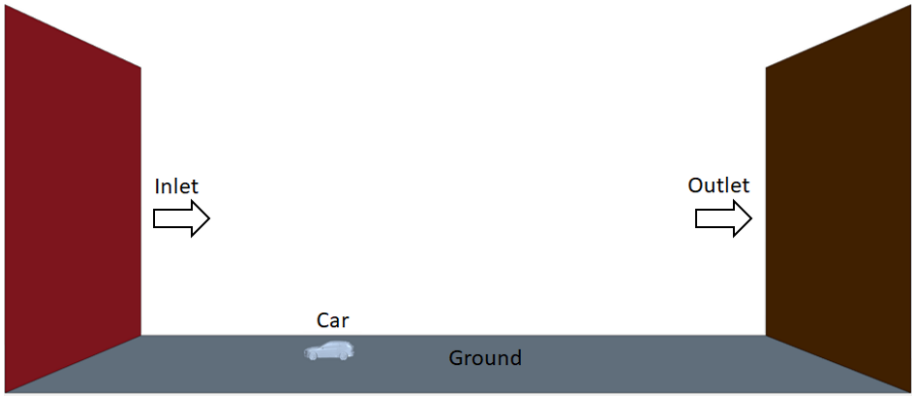

Figure 3.8: Representation of the domain and boundaries

The aerodynamics group at VCC have developed the aero_vcacp scripts which automates the entire CFD simulation and post-processing. The scripts are split into 4 sections, namely: prep, mesh, run and post. The prep script imports geometry, creates domain, performs surface wrapping, surface meshing and sets various other settings such as coordinate systems, auto mesh settings, boundary settings and so on. The mesh script performs volume meshing in the domain. The run script is used to create various reports, monitors and plots and runs the simulation based on the settings prescribed. And finally the post script does post-processing based on user input and is capable of representing scalars, vectors, surfaces and iso-surfaces.

The result of the prep and mesh scripts contains the volume mesh of the fluid domain. The domain has about 253 million cells. The mesh is refined close to the body of the car and in the region of the wake behind the car. The mesh is also refined close to the wheels to capture the turbulent air streams entering and exiting the wheel. The Fig. 3.9 represents the mesh along the x-z plane and y-z plane.

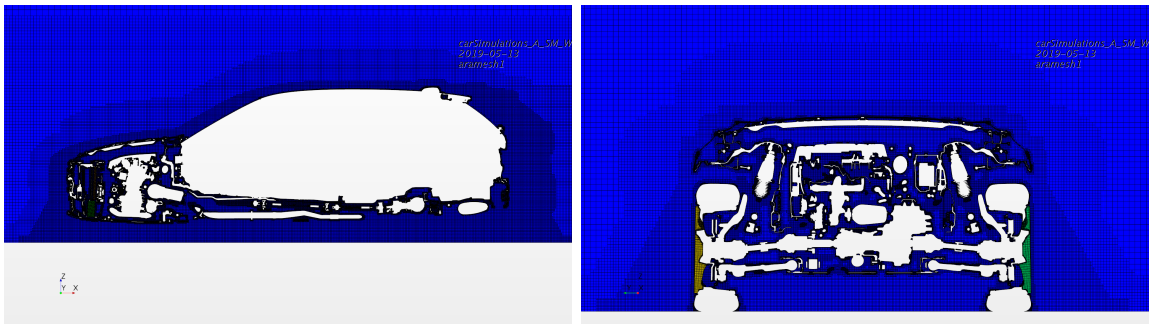

(a) Mesh plane about the y axis

(b) Mesh plane about the x axis near the front wheel

Figure 3.9: Mesh planes about x-axis and y-axis

The wheel setup consists of an 18-inch wheel with slick tyres as shown in Fig. 3.10. A subtract is created in Star-CCM+ between the rims and the sliding mesh region. The region represented by the transparent blue color in the figure is the sliding region. The region is rotated about the corresponding wheel axis. The wheel setup is modelled by using sliding mesh approach to the rims spokes and rotating wall to the tyres. Since the tyre geometry is slicks, rotating with rotating wall method is valid and easy to setup.

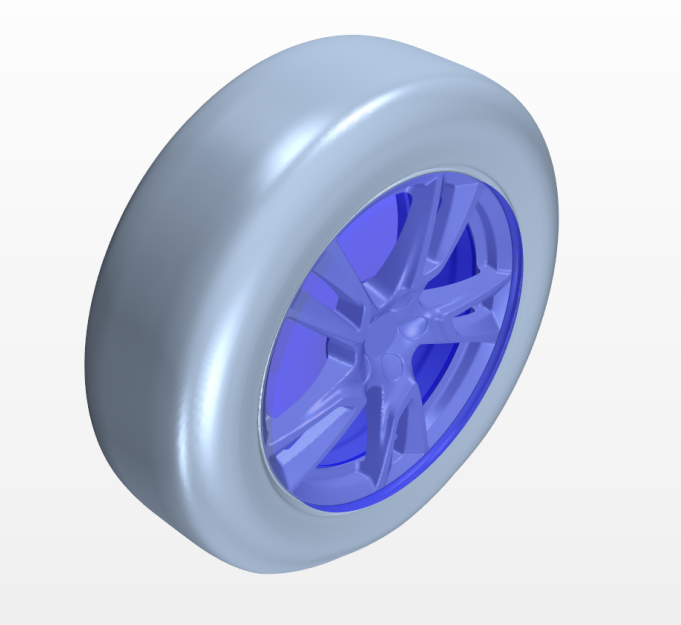

Figure 3.10: Wheel setup

The simulation was performed in steps where a steady state case was run initially to achieve faster convergence in transient simulations. Then the time step was slowly ramped to finer values in steps and the number of iterations per timestep was decreased slowly.

- Steady state simulation for 1500 iteration. Then the physics was changed to unsteady.
- Δt=5e-3s for 0.1s with 20 iterations per timestep with velocity URF=0.7 and pressure URF=0.25.
- Δt= 5e-3s till 2s with 10 iterations per timestep with velocity URF=0.8 and pressure URF=0.4 (URFs were unchanged henceforth).
- Δt=1e-3s till 2.4s with 8 iterations per timestep.
- Δt=2.5e-4s till 2.5s with 8 iterations per timestep.
- Δt=2.5e-4s till 4s with 6 iterations per timestep.

With this ramping of timestep and iterations, the flow reached a fully developed condition faster. Various reports were setup such as C_d, C_dA, C_lr, C_lf, time per iteration and time per timestep to evaluate the performance of the car and the simulations. Averaging was performed between 2.6s and 4s.
The setup described above was considered as the baseline configuration. Four studies were made in comparison to this.

- Comparison between SM and MRF methods to model wheel rotation.
- Flow field comparison when using open rims and closed rims.
- Time step dependency study.
- Interface splitting across the sliding interface.

In the first study, wheel modelling approaches were investigated. The same CAD geometry was used in evaluating both the SM and MRF approaches. In the SM approach, the region was modelled using rigid body motion where the mesh physically moves and in the MRF approach, it was modelled in reference frames so, it accounts for the motion numerically.
In the second study, the difference between open and closed rims were investigated. In the same wheel setup as the baseline, a rim cover was modelled in ANSA and surface meshed. In this study only SM approach was used. The two rims, open and closed rims are shown in Fig. 3.11.

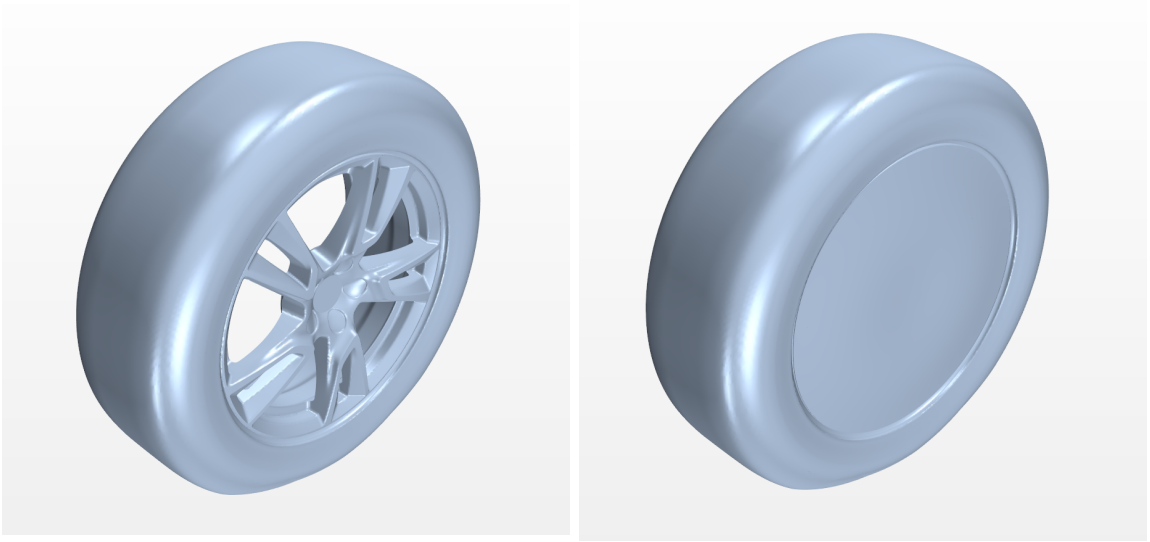

(a) Open rim **(b)** Closed rim

Figure 3.11: Configuration of wheels

Next, the time step dependency was checked. Two time steps were used for this study. First was the default value of 2.5e-4s which was setup the same was the first study and the second case used a finer Δt of 1e-4s. 2.5e-4s was used for the reference simulation because it was the only affordable timestep. The same ramping settings was used for the case with 1e-4s for simplicity. But the settings were slightly altered towards the end to ease the simulation into 1e-4s. The timestep of 2.5e-4s with 6 inner iterations was run till 2.55s and then changed to 1e-4s till 4.1s. The time averaging of the reports and fields happened between 2.7s and 4.1s. This additional 0.15s in the beginning (from 2.55s to 2.7s) is to allow the solution to stabilize in the new timestep of 1e-4s. The forces and Courant number in the domain were compared between the two cases.
Finally, like in the previous section with the cylinder, the sliding region's interface was split into three faces in ANSA v.18 to see if speed up occurs. Fig. 3.12 shows

the front left wheel in the baseline configuration and when split into different PIDs. Using Java scripts, these different PIDs were created as separate boundaries in Star-CCM+ and interfaced in boundary mode. This was done to all the SM regions corresponding to the 4 four wheels of the car.

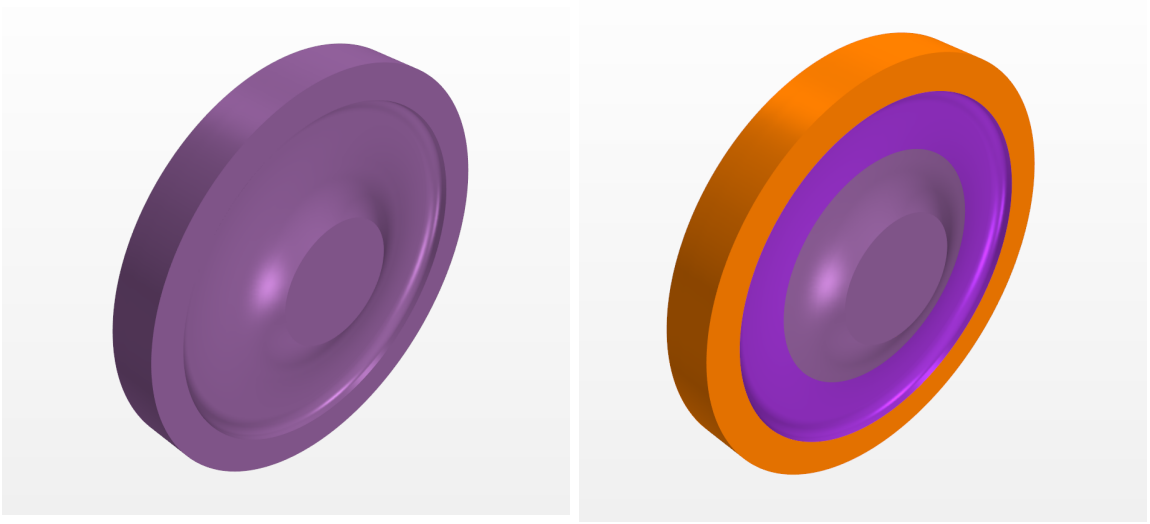

(a) 1 interface on the sliding mesh region of the wheel

(b) 3 interfaces on the sliding mesh region of the wheel

Figure 3.12: Geometry of the wheel's SM region used in the study

4

Results and Discussions

In this chapter, the results are presented in the following way: the solution for the cylinder simulations are presented first which includes analysis of the flow field, verification of results from the RW and SM simulations, parametric mesh and timestep study and finally the results from splitting the interface. In the second part, the flow field around the car is analyzed. Then the results from different approaches of wheel modelling are evaluated, followed by the open and closed rims' effects on the flow field. The time step dependency study conducted on the car is presented. Finally the results from the interface splitting and its influence on the time of the simulation time is discussed.

4.1 Cylinder simulations

4.1.1 Analysis of flow field

The flow around the rotating cylinder is analyzed in this section, the setup was explained in section [3.1]. The results shown in this section are based on RW method. The Fig. 4.1 represents the mean of velocity field. The velocity decreases gradually as the flow reaches the cylinder as it resists the flow. The flow accelerates as it passes over it. The downstream side of the cylinder is dominated by a wake which results in vortex shedding(vortex shedding is not seen in Fig. 4.1 because it represents time averaged velocity field). Vortex shedding is characterized by flow detaching from a bluff body in an oscillating fashion. This causes the body to experience alternating forces.

The wake is the result of the development of flow separation behind the bluff body, cylinder in this case. A wake region is characterized by reduced velocity and reversed flow and vortices as seen in the figure. Flow separation is marked by a separation point. There are two such points, one on the top and bottom of the cylinder. Separation occurs depending on pressure recovery and boundary layer development. It is noted that the flow accelerates more on the lower side of the cylinder because of rotation. The oncoming flow is opposite in direction to the tangential velocity of the cylinder on the upper side of the cylinder. So, the resulting velocity is very low in magnitude whereas on the lower side, it is almost double the freestream as the velocity vectors are parallel. Additionally, the cylinder rotation causes the vortex shedding to occur slightly inclined to balance the flow. The separation point on the top of the cylinder is more upstream than the bottom which is also due to rotation.

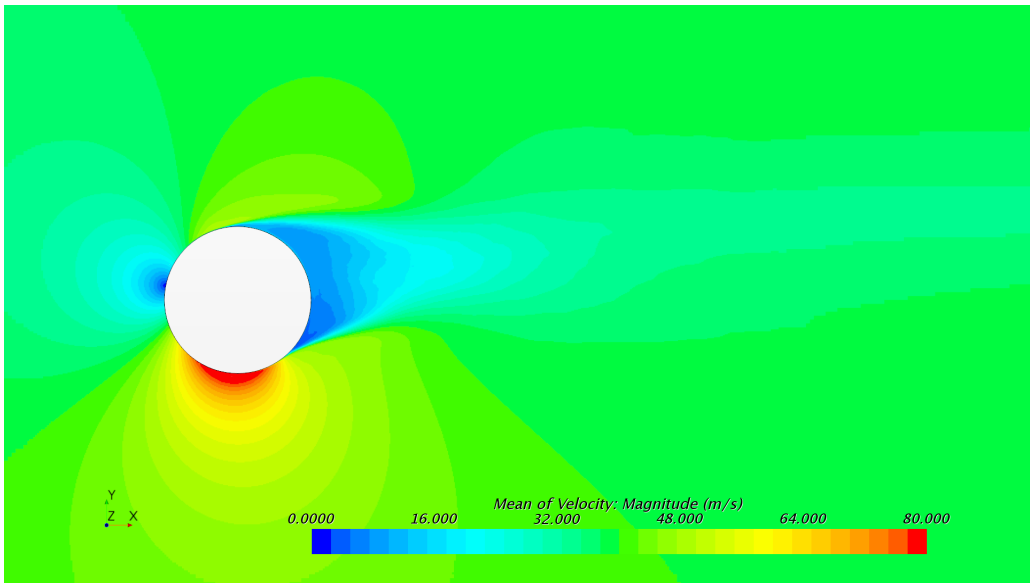

Figure 4.1: Mean velocity field around the cylinder from RW method

Fig. 4.2 gives the mean velocity along the line probes defined in the domain as shown in Fig. 3.3. As the downstream side of the cylinder is dominated by the wake, the velocity close to the cylinder is low (the red line in Fig. 4.2) but gradually recovers as the flow moves further away from the cylinder wall. The shift in the velocity profiles towards the right side is due to the rotation of the cylinder.

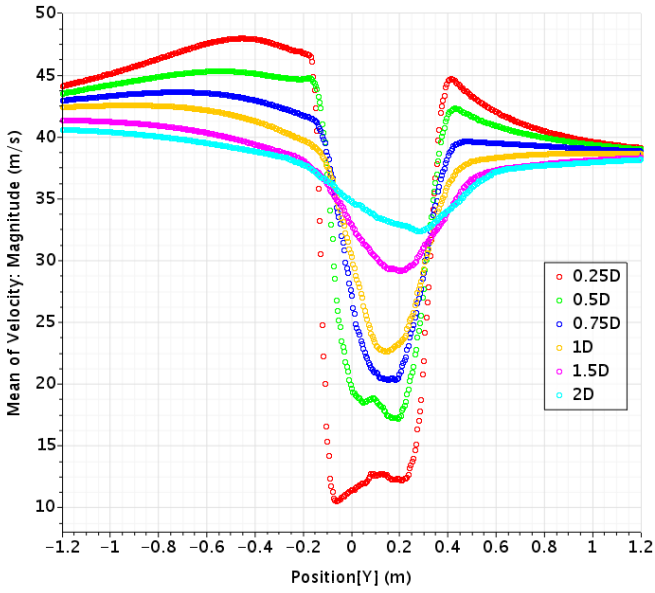

Figure 4.2: Mean velocity plot along the line probes from RW method

Fig. 4.3a and Fig. 4.3b represent the forces, drag and lift, acting on the cylinder and Fig. 4.4, the moment. The simulation being transient and since a DES model was used to resolve the turbulence, the forces and moment are fluctuating continuously in time. So time averaging was performed for all the quantities which is marked by

the green line in the plots. The mean values of each of the quantities are shown in table. 4.1.

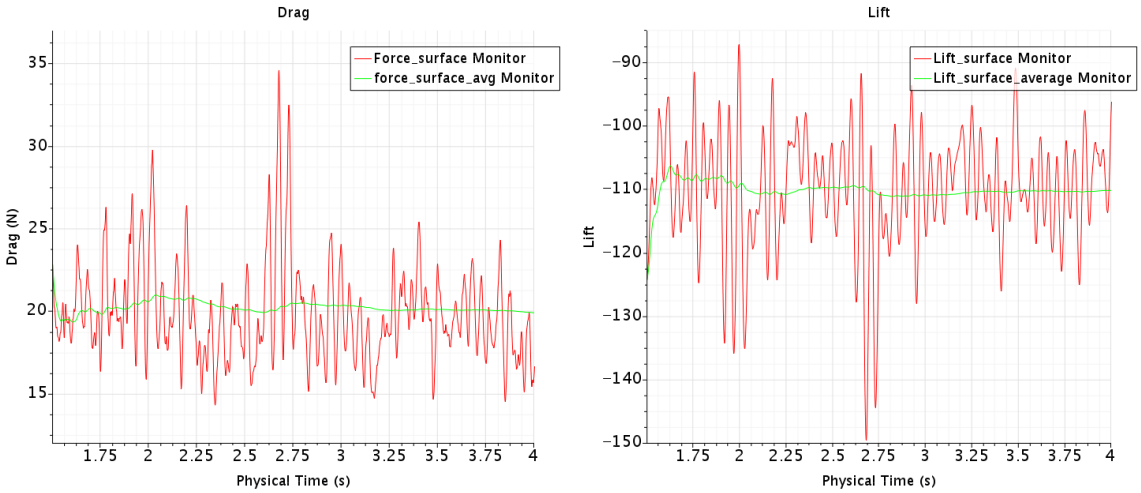

(a) Drag force acting on the cylinder sur-**(b)** Lift force acting on the cylinder surface face

Figure 4.3: Forces acting on the cylinder

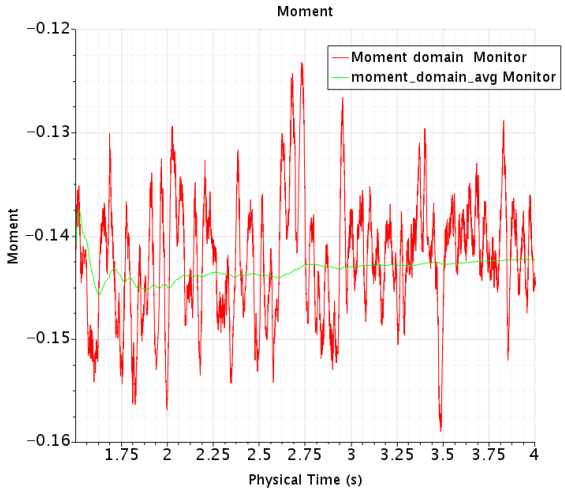

Figure 4.4: Moment in the rotating region

Quantity	Mean value
Drag (N)	19.9
Lift (N)	-110
Moment (Nm)	-0.142

Table 4.1: Mean forces acting on the cylinder and moment acting in the domain

Remark

From Fig. 4.2, it can be seen that the gradients of velocity are very high in the wake and high spatial discretization is required to achieve good results. But high spatial discretization imposes a restriction on the temporal discretization also. Hence, the CFL condition had to taken into account and as a condition, it is restricted to a low value(<5). With vortex shedding involved, it was essential to take into account the shedding frequency and it was found to be 28.5Hz based on Delany and Sorensen's relationship between Re and Strouhal number[24]. By taking all that into consideration, a timestep with Δt=1e-5s was required for the simulation.

4.1.2 Comparison between RW and SM methods

With the setup given in section 3.1 and a timestep of 1e-5s, both RW and SM methods were tested on a rotating cylinder. Fig. 4.5 shows the means of velocity along the line probes. It can be seen from this figure that both velocity profiles look similar. The velocity profiles closer to the cylinder appear slightly different but as the flow moves downstream, the errors evened out.

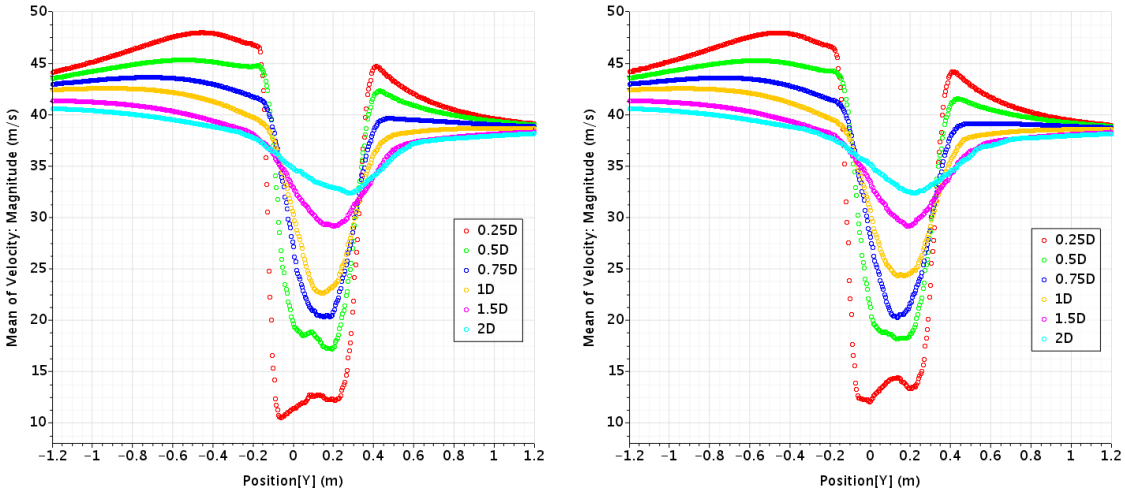

(a) Rotating wall method **(b)** Sliding mesh method

Figure 4.5: Mean velocity along the line probes comparing RW and SM

A $\frac{\Delta V}{V_{in}}$ plot was created where $\Delta V = V_{RW} - V_{SM}$ as seen in Fig. 4.6. We can observe a small shift in the velocity profile across the domain along the line probes 0.25D and 0.5D but beyond that, the errors are very small. This is clearly marked in the plot by two peaks on those two corresponding velocity profiles. A possible reason for this shift in velocity profiles is due to insufficient temporal discretization and more about it is explained in section 4.1.3.

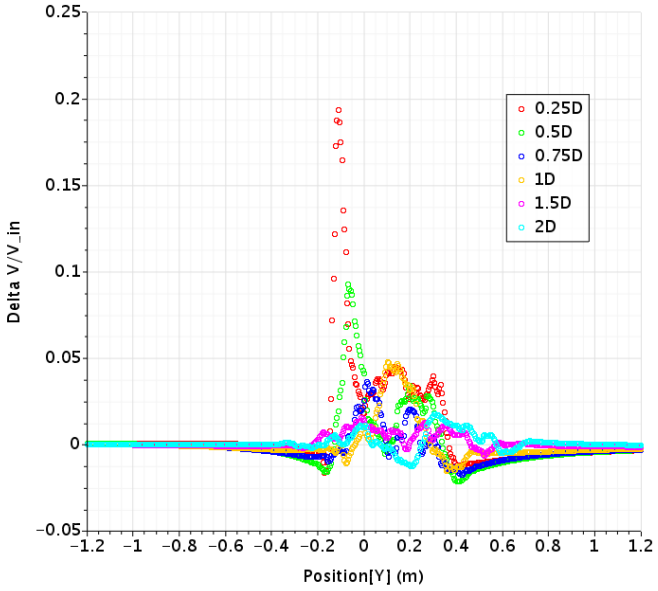

Figure 4.6: $\frac{\Delta V}{V_\infty}$ plot comparing RW and SM methods

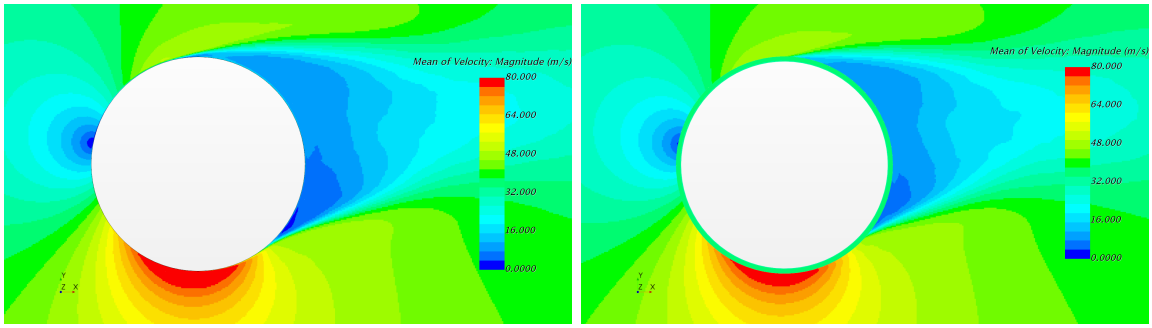

(a) Rotating Wall **(b)** Sliding Mesh

Figure 4.7: Mean velocity around the cylinder comparing RW and SM methods

Fig. 4.7 represents the scalar scene of RW method and SM method. It can be seen that both the scalars look very similar. In the region where the mesh moves in SM method, the velocity value is averaged due to mesh motion and it cannot be read accurately with the current setup.
The forces acting on the surface of the cylinder and the moment in the domain were monitored and their mean values were calculated for both the methods. Table 4.2 shows that the mean values of these quantities are very close to each other.

Quantity	RW	SM
Drag (N)	19.9	19.8
Lift (N)	-110	-113
Moment (Nm)	-0.142	-0.146

Table 4.2: Means of forces and moment comparison between RW and SM approaches

Remark

The RW method took 90 hours and SM method took 206 hours on 1000 cores for the simulation to complete. This increase in time for the latter method is due to the physical motion of the mesh for each time step. This proved to be extremely costly and impractical. So a parametric study was carried out to see how much the mesh, timestep and the geometry of the rotating region of SM affect the final solution.

4.1.3 Parametric Study on SM method

Different settings were tested and a suitable setup has been finally suggested which is computationally cheaper and has comparable results to the base case. Based on the settings as given in Table. 3.2, each parameter was modified from the base case and the results were compared. All simulations (including ¨Base case¨ in the figures) were performed with 1e-4s timestep unless stated otherwise (for practical reasons).

Fig. 4.8 presents the results for the time averaging study and time step dependency study. It can be seen that averaging the solution to 4s and 5s, both yielded the same results. Hence it can be inferred that, averaging the solution to 4s is sufficient. The mean of the forces and moment did not stabilize until around 3.5 and so it is essential to run the simulation for a physical time of atleast 4s. From the same figure, it can be seen that the mean velocity profile shifts towards the right side with coarsening the time step. This was initially construed to be because of mesh motion interpolation and/or courant number effects. But, in the case with cell size 4mm and a time step of 2e-4s, the courant number is relatively preserved as compared to 2mm cells with 1e-4s timestep. This was able to produce results with minimal shift. Thus it can be stated that, the shift in the profiles is due to courant number. Hence it is essential to maintain a good value of CFL number in the cells. The results produced by the the simulation with 4mm cells was erroneous as the cell size was too coarse to resolve the flow. In Fig. 4.6, it was observed that there was a similar shift in velocity profiles for SM as compared to RW simulations. It is possible that the timestep must be further refined for SM to achieve the same solution as RW. But considering how expensive the SM method is, it was decided not to do so.

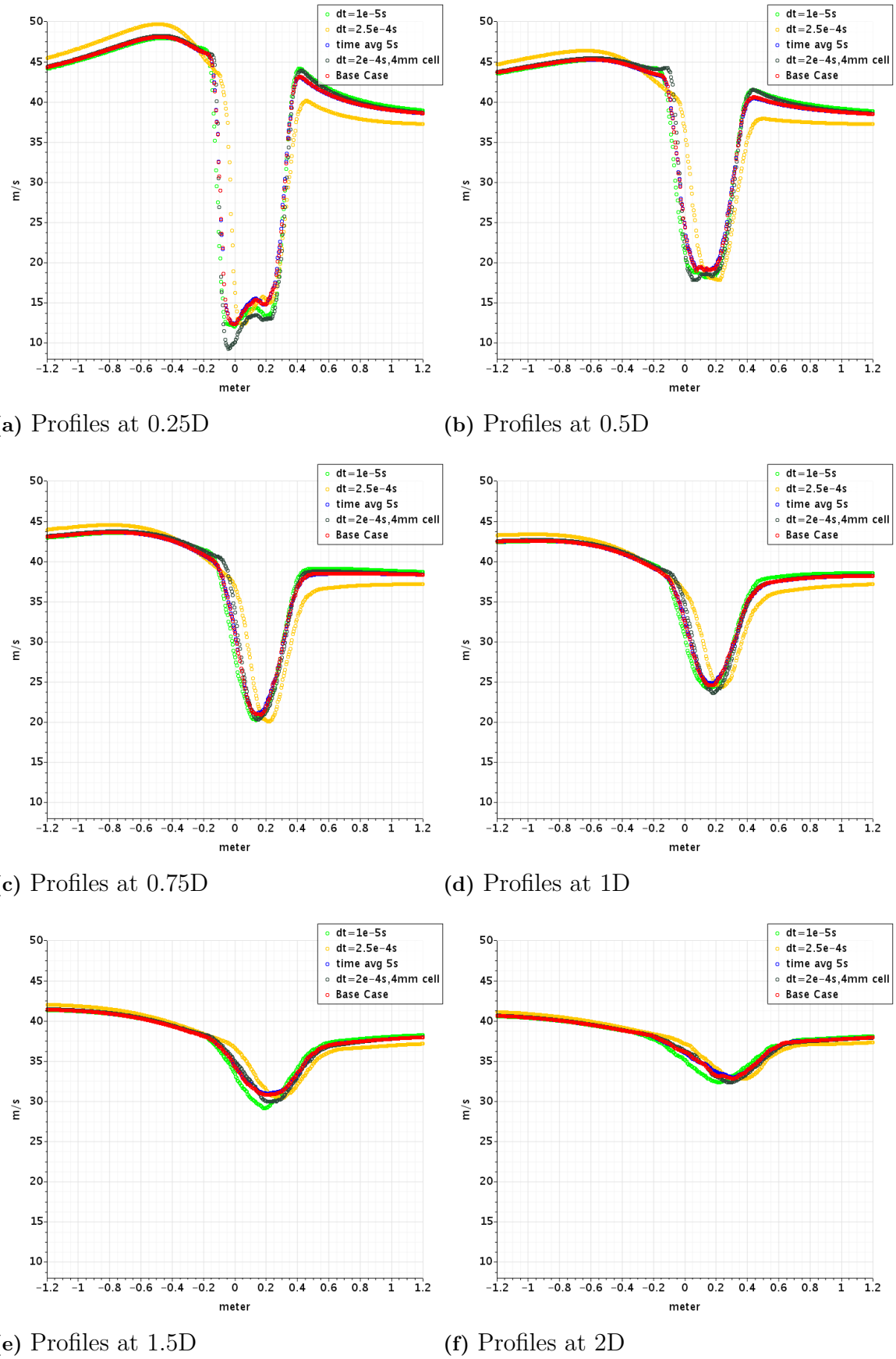

(a) Profiles at 0.25D

(b) Profiles at 0.5D

(c) Profiles at 0.75D

(d) Profiles at 1D

(e) Profiles at 1.5D

(f) Profiles at 2D

Figure 4.8: Parametric study results from different parameters in comparison with the base case

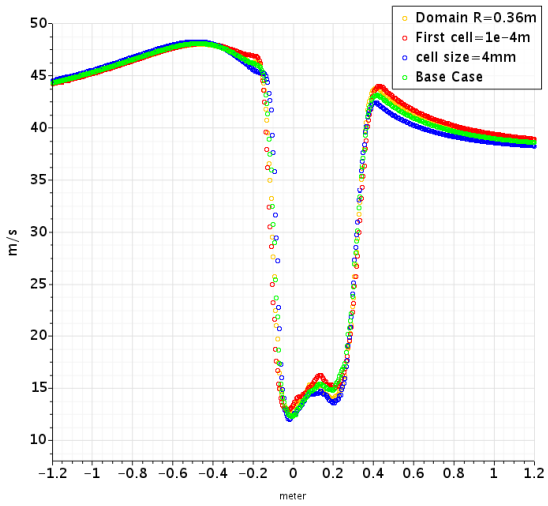

(a) Profiles at 0.25D

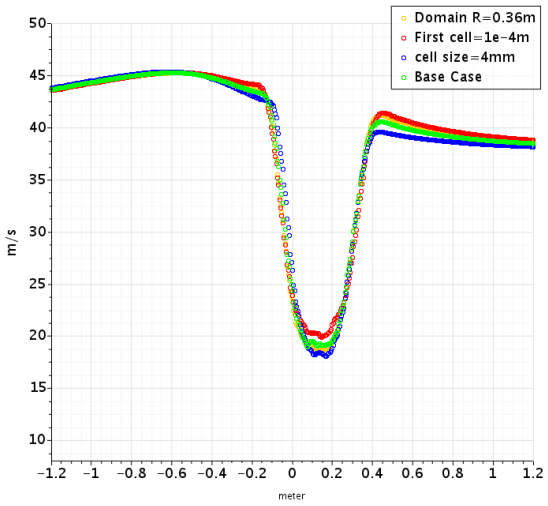

(b) Profiles at 0.5D

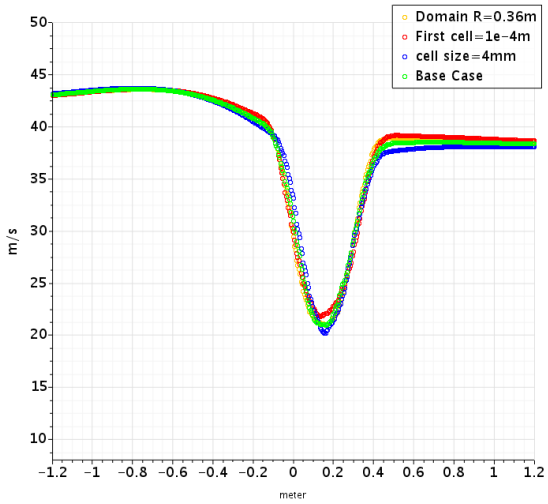

(c) Profiles at 0.75D

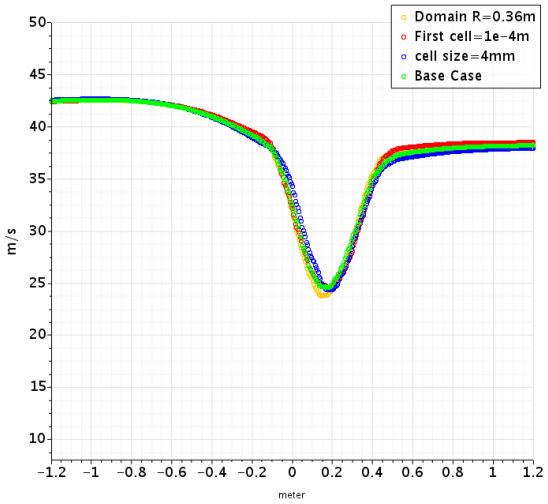

(d) Profiles at 1D

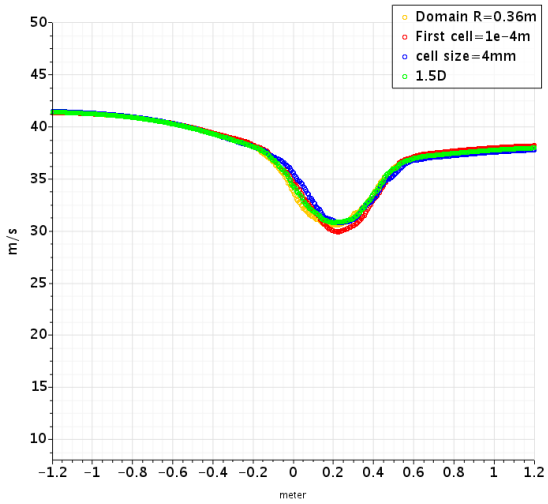

(e) Profiles at 1.5D

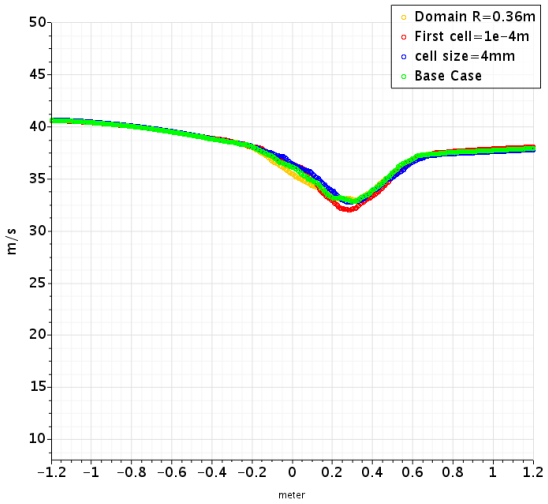

(f) Profiles at 2D

Figure 4.9: Parametric study results from different mesh and geometry settings in comparison to the base case

The Fig. 4.9 shows the dependency of cell size at the wall, y+ values and the size of the rotating domain in this case. It can be seen that the profiles were slightly offset from each other. Coarsening the cell size to 4mm at the wall and having a high y+ value at the wall produced poor results because the gradients near the wall and in the wake region were very high and these coarser settings was not capable of predicting them properly. This resulted in poor accuracy on the forces and moments. Enlargening the domain size yielded very similar velocity profiles and forces that were close to the solution from the finest settings (with $\Delta t = 1e - 5s$).

Finally, Fig. 4.10 represents mean velocity field obtained from a coupled solver and wake refined mesh running segregated solver in comparison to the base case. It can be seen that all the cases yielded similar results close to the wall. But away from the wall, wake refinement under-predicted the velocity means. Solving with coupled solver proved to be challenging due to certain instabilities in forces. Hence the segregated solver proved to be the more reliable choice. Wake refinement produced similar results as compared volume refinement around the cylinder. This proved to very useful because the wake refinement reduced the number of cells in the domain by around 35% as compared to using volume refinement.

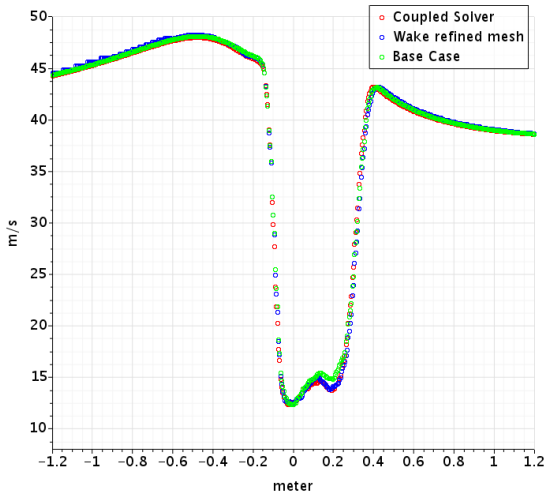

(a) Profiles at 0.25D

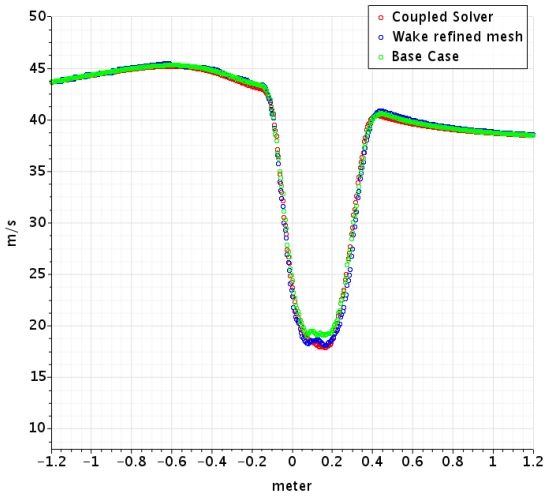

(b) Profiles at 0.5D

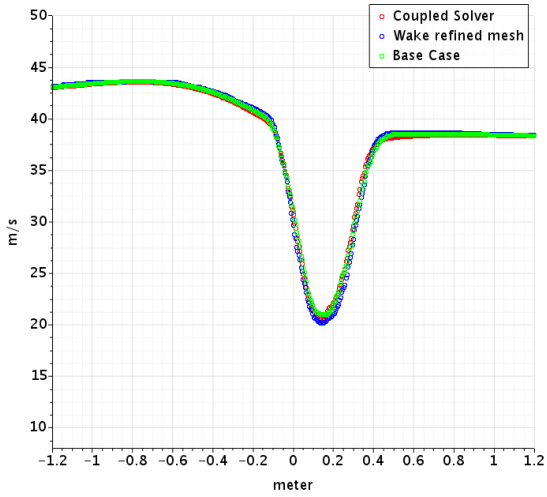

(c) Profiles at 0.75D

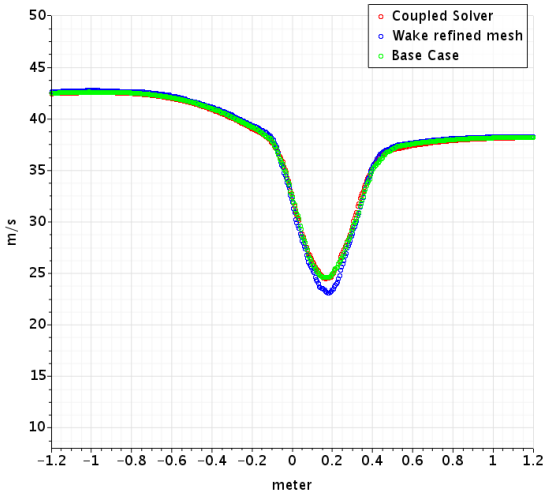

(d) Profiles at 1D

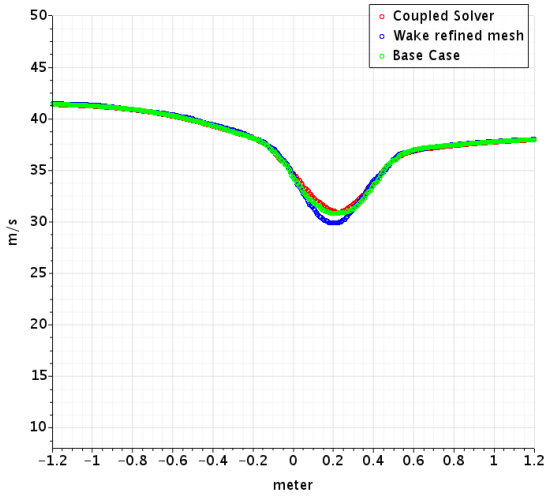

(e) Profiles at 1.5D

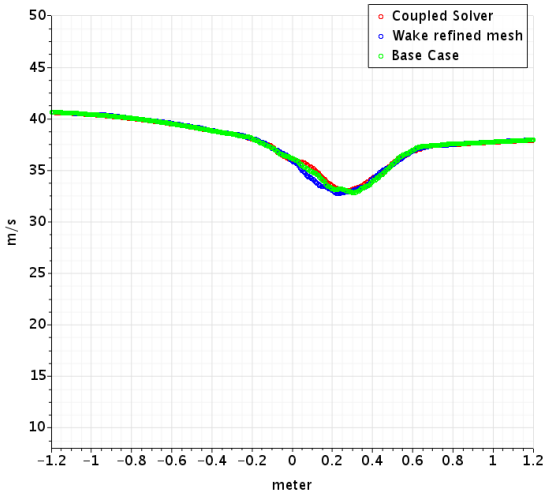

(f) Profiles at 2D

Figure 4.10: Parametric study results from coupled solver and wake refinement as compared to the base case

With these results, the best configuration to run the case using SM method was be with the following setup:

- Time step - 1e-4s
- Total physical time - 4s
- cell size at the wall - 2mm
- 14 prism layers with first cell height of 1e-5m, growth ratio of 1.5 and height 6mm.
- Rotating domain radius - 0.36m
- 4mm cell size wake refinement for 2.4m with 8 degrees inclination and spread angle of 10 degrees.

The resulting mesh is represented in Fig. 4.11. The solution from the mesh is shown in Fig. 4.12 which is compared to the solution with the finest settings. Fig. 4.13 represents the $\frac{\Delta V}{V_{in}}$ for the solution in Fig. 4.12. Table 4.3 compares the forces, moment in the domain and time taken for simulation between RW method, the SM method with the base setup and the newly suggested setup.

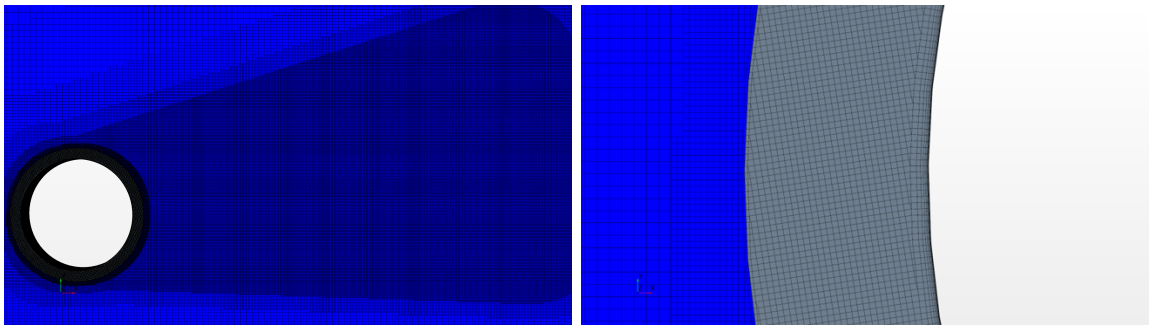

(a) Wake refinement downstream of the cylinder **(b)** Enlarged view of the rotating region

Figure 4.11: Final mesh representation

Quantity	**RW**$_{base}$	**SM**$_{base}$	**SM**$_{final}$
Drag (N)	19.9	19.8	19.5
Lift (N)	-110	-113	-115
Moment (Nm)	-0.142	-0.146	-0.146
Time for simulation (hours)	90	205	22.5

Table 4.3: Force, moment and time comparison for different cases

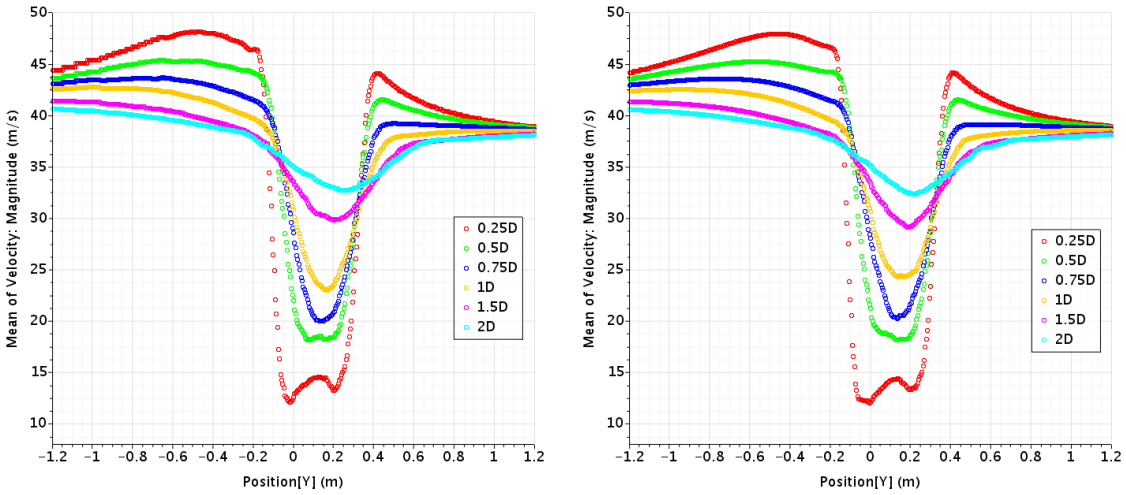

(a) Mean velocity profiles from the final mesh

(b) Mean velocity profiles from the finest SM configuration

Figure 4.12: Mean velocity profiles along the line probes comparing the base and final configuration

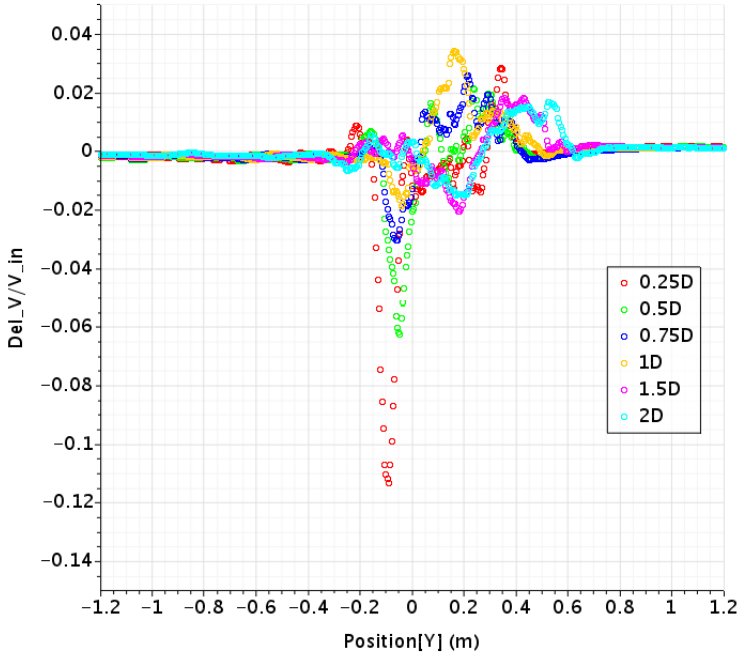

Figure 4.13: $\frac{\Delta V}{V_\infty}$ plot of SM solutions

It can be seen from this figure that the although there is a small shift in the solution due to the coarser time step, the degree of error is low with an average error of +/- 4%.

4.1.4 Splitting interface - Pseudo-parallelization

In this section, the results from the simulation carried out by splitting the interface of the cylinder into a number of boundaries are presented. The setup is as explained in section 3.1 and as shown in Fig. 3.6.

The modification to the setup did not change the final solution. But it did bring about a considerable change in the simulation time. Fig. 4.14 shows the change in time per timestep as a function of the number of interfaces. Fig. 4.14a represents the relation between avg. time per timestep and the number of interfaces while Fig. 4.14b shows the percentage reduction in time per timestep with the number of interfaces.

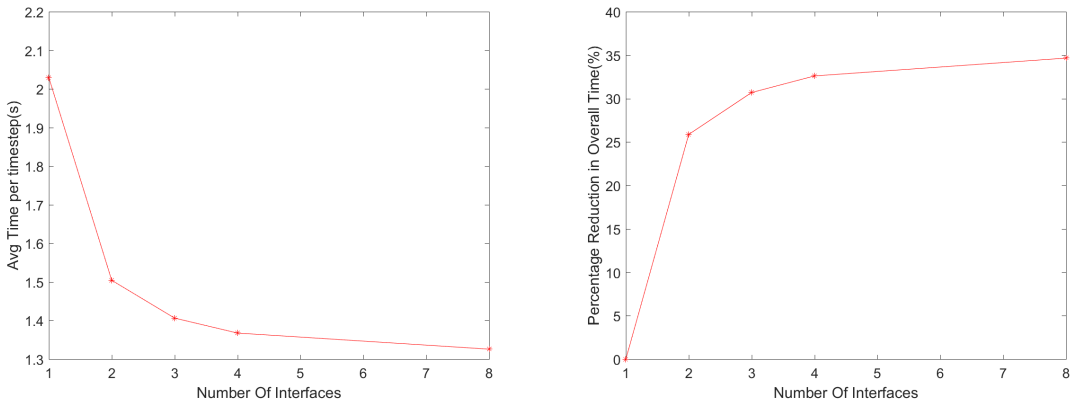

(a) Avg time per time step vs Number of interfaces

(b) Percentage reduction in avg. time per timestep vs Number of interfaces

Figure 4.14: Effect on avg. time per timestep

It can be seen that, the avg. time per timestep decreases with increase in the number of interfaces. When using 8 interfaces, the time reduces from 2.02s (for single interface) to 1.32s per timestep which is about 35% reduction in the overall simulation time.

The time taken for updating the interfaces is the difference between the time per timestep and sum of iterations per timestep. Fig. 4.15a represents the effect this method had on the time for updating interfaces and Fig. 4.15b represents the percentage reduction in the updating time. From the figures, it is seen that the updating time of 1.15s for one interface decreased to 0.366s for 8 interfaces, which is about 68% decrease.

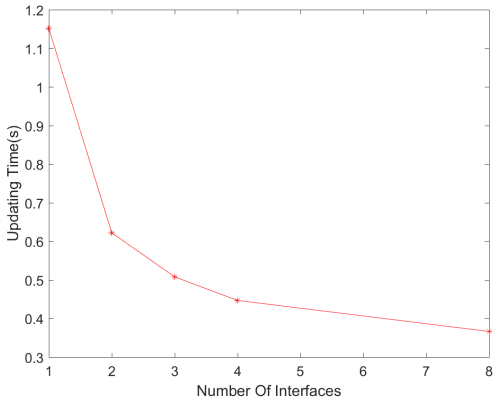

(a) Avg mesh updating time per time step vs Number of interfaces

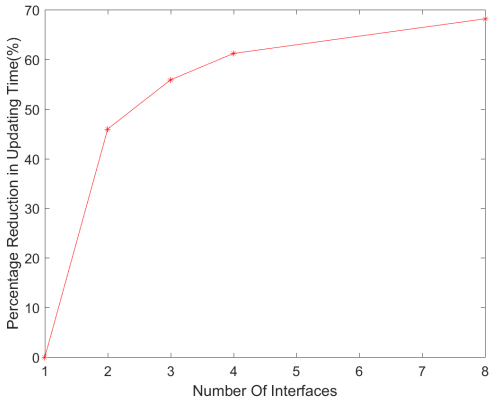

(b) Percentage reduction in avg. mesh updating time per timestep vs Number of interfaces

Figure 4.15: Effect on avg. updating time per timestep

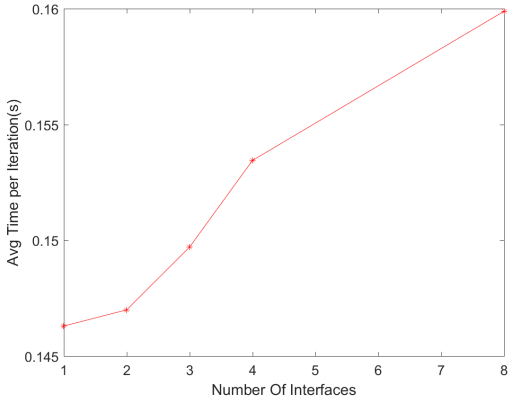

(a) Avg time per iteration vs Number of interfaces

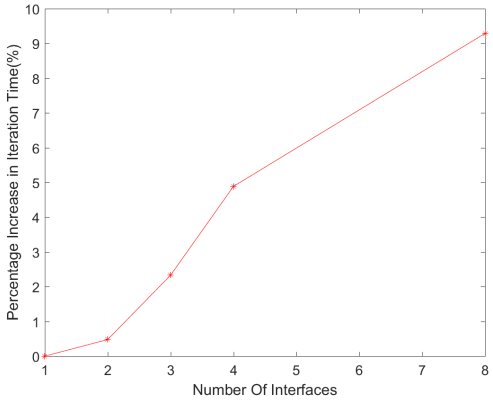

(b) Percentage increase in avg. time per iteration vs Number of interfaces

Figure 4.16: Effect on avg. time per iteration

Additionally it was noted that, this method had an effect on the time per iteration. Fig. 4.16a denotes the effect this method had on the time per iteration and Fig. 4.16b, the percentage change in the time per iteration. It is evident from the figures that an increase in number of interfaces caused almost a linear increase in the time

per iteration. With 8 interfaces, around 9% increase was noted. A increase in the number of boundaries increases the iteration time. Additionally the solution updating at the beginning of each timestep across the interface takes more when boundary mode interfaces are used instead than contact mode interfaces. So, the first iteration takes slightly more time than the rest, thus increasing the mean iteration time. This increase in time for the first iteration is proportional to the number of interfaces.
Fig. 4.17 compares time taken for each step of SM operation in a timestep with the configurations using 1 interface and 8 interfaces. Each timestep has a mesh updating step followed by 6 iterations. It can be seen that while using 8 interfaces, the mesh updating step is optimized by about 0.8s. The time per iteration increases slightly with higher number of interfaces but it is negligible as compared to the time gained from the updating step.

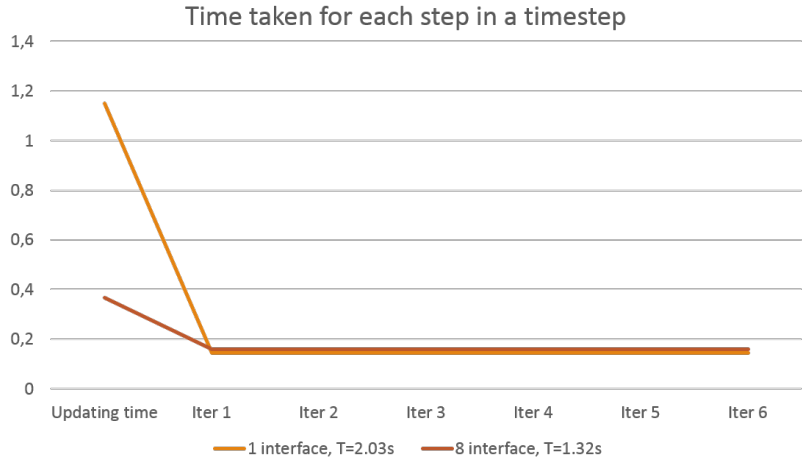

Figure 4.17: Comparison in the time taken for each step in a timestep between 1 interface and 8 interfaces

The results from the study are summarized in Table. 4.4. It is quite evident that increasing the number of interfaces, reduced the time per timestep. But it is noted that while the time per timestep decreases, time per iteration increases. So beyond a point, even if the updating time was very low, time per timestep could increase. From Table. 4.4, it is seen that the decrease in time between 4 interfaces and 8 interfaces is 0.04s, which is quite small. So, optimizing the number of interfaces is important for the application.

Parameter	**1 int.**	**2 int.**	**3 int.**	**4 int.**	**8 int.**
Time per timestep (s)	2.02	1.50	1.41	1.36	1.32
Time per iteration (s)	0.146	0.147	0.150	0.153	0.160
Updating time (s)	1.15	0.622	0.508	0.447	0.367

Table 4.4: Summary of pseudo-parallelization study

Thus, pseudo-parallelization approach can be used for SM applications to speed up the mesh updating step.

Summary of cylinder simulations

Simulations were performed to understand the behaviour of RW and SM methods to model rotation. Since the case was very mesh and timestep dependent, a parametric study was carried out and a configuration with coarser settings was suggested that could yield acceptable results. Finally, pseudo-parallelization approach was tested and it was found that this method can be used to speed up SM applications such as, a complete car setup with rims modelled using SM method.

4.2 Car simulations

4.2.1 Car aerodynamic analysis

Fig. 4.18 represents the mean velocity field of the flow on the plane at y=0(centre of the car). It can be seen that the flow at the front end of the car is decelerated due to presence of the front shutters and the bumpers. This effect is carried upstream. The flow along the upper body get accelerated slightly more than the under body by continuity principle. The rear end of the car is dominated by the wake that is characterized by the low velocity, re-circulation and vortex shedding.

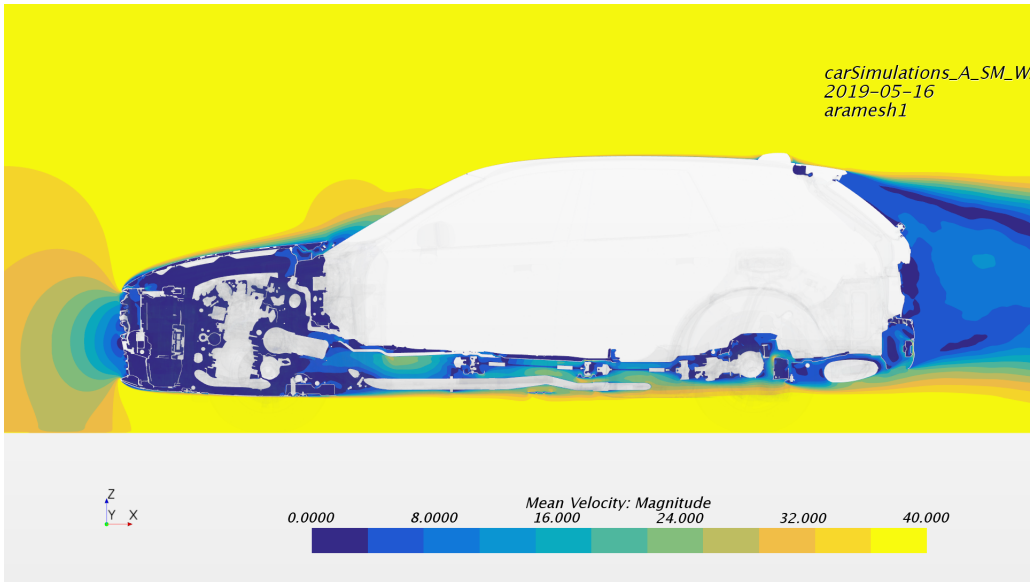

Figure 4.18: Mean velocity field around the car about the plane y=0

For a car on the road, the flow enters the front shutters which is essential for cooling flow and it tracks through the engine and the power train. This causes pressure build up in the engine bay which is poor for the aerodynamics of the car but essential for the functioning of the car. In this simulation, as seen in Fig. 4.18, the front shutters are closed and so the flow does not enter the engine bay.

Fig. 4.19 represents the mean C_p on the surface of the car. C_p is the coefficient of the pressure and it is used to characterize fluid motion. A higher C_p value indicates that the flow decelerates towards the surface and it usually occurs when the flow is perpendicular to a surface. A lower C_p value marks acceleration of the flow or flow separation. From the figure, it can be seen that the front shutters, front part of the side mirrors and the bottom of the windshield are marked as high pressure regions as they are surfaces perpendicular to the flow and causes the flow to slow down. Whereas the roof, A-pillar, the side bumpers and the front wheels are marked by very low C_p values which means the flow accelerates and/or separates in these regions.

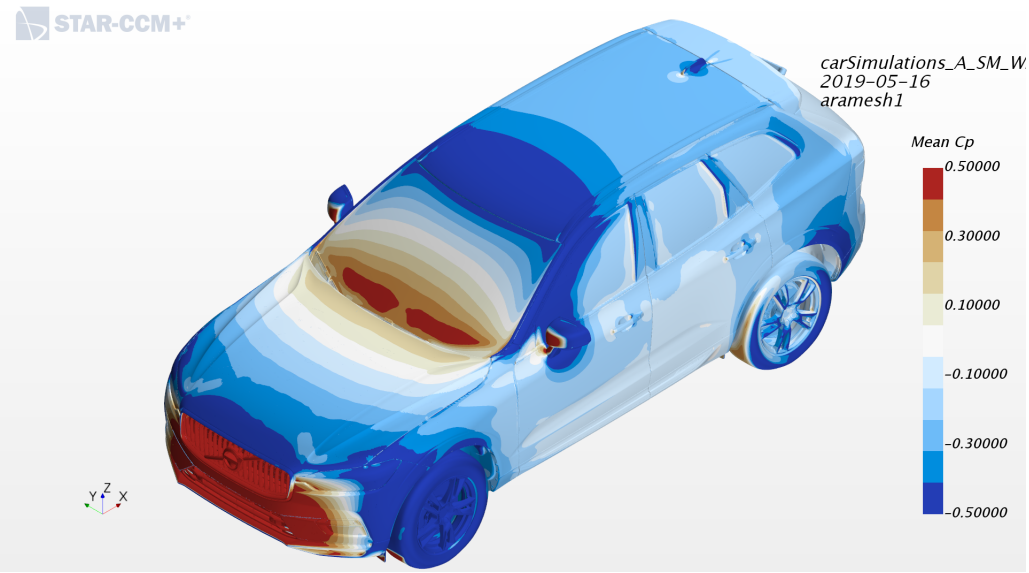

Figure 4.19: Mean C_p on the surface of the car

C_p is an important parameter because it is represents where the forces act on the body of the car. The drag force is calculated by integrating the C_p over area normal along x-axis, over the car. And similarly the lift/downforce is calculating by integrating pressure over area normal along z-axis. Fig. 4.20 represents C_p on the base of the car. This is important because, the difference between F_x on the front end consisting of the front shutters, bumpers, windshield and the rear as shown in fig. contribute to the drag. So higher the C_p at the base of the car, lower the drag.

Figure 4.20: Mean C_p on the rear end of the car

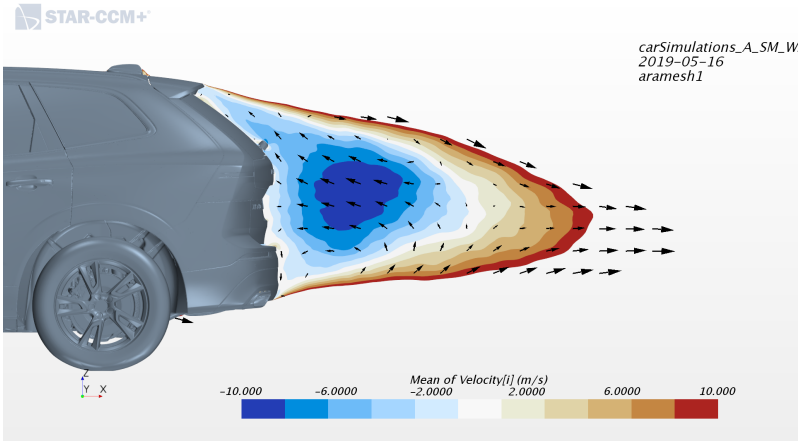

(a) Mean velocity vector about the plane y=0m

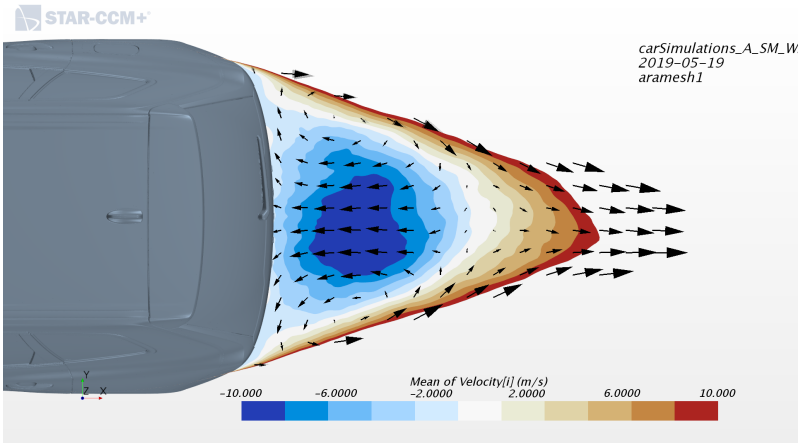

(b) Mean velocity vector about the plane z=1m

Figure 4.21: Mean velocity vector field representing the wake behind the car

The large wake behind the car is one of the most important features to be considered while analyzing the aerodynamic performance of the car. Fig. 4.21a and Fig. 4.21b represent the velocity vectors behind the car along the planes y=0 and z=1m. It can be seen from these vectors that a strong reversed flow is experienced in this region. A balanced wake is beneficial for the stability of the car. From Fig. 4.21a, it can be seen that the base wake is imbalanced along the z-direction. This is the effect of flow from the roof and the underbody profile of the car. The flow from these surfaces greatly affect the shape, size and balance of the base wake. In this case, it can be seen that flow experiences an upwash. From Fig. 4.21b, it can be seen that the re-circulation near either sides of the car is balanced almost equally. This means that the car does not have lateral flow instabilities.
The CFD simulations need to be bench-marked for accuracy with experimental results. The most important parameters that define a car's aerodynamic performance are C_d, C_lr, C_lf and C_dA. The table 4.5 represents the Δ=Exp-CFD for C_d and C_dA. The other two variables for the lift are not considered from experimental data because appropriate correction for road effects and contact patch had not been done. But even with C_d and C_dA, it was helpful in establishing the accuracy of the results presented in the project.

Quantity	$\Delta = Exp - CFD$
C_d	-0.001
C_dA	-0.005

Table 4.5: Δ of various aerodynamic parameters of Experimental data and CFD data

It is to be noted that the experimental test was done on the same car with production tyres while the CFD simulation considered slick tyres. It is known that, detailed tyre profile affects the overall drag on the vehicle. There are always discrepancies between experimental and numerical results due to leakages on surfaces, blockage effects of the wind tunnel and so on. So, it can be established that the results are within an acceptable level of accuracy.

4.2.2 Wheel aerodynamic analysis

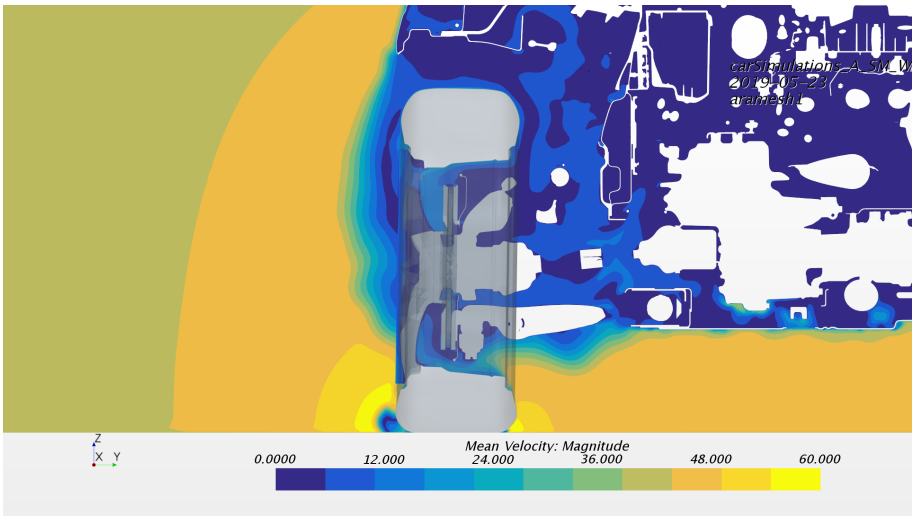

(a) Mean velocity field across the centre of the front wheel

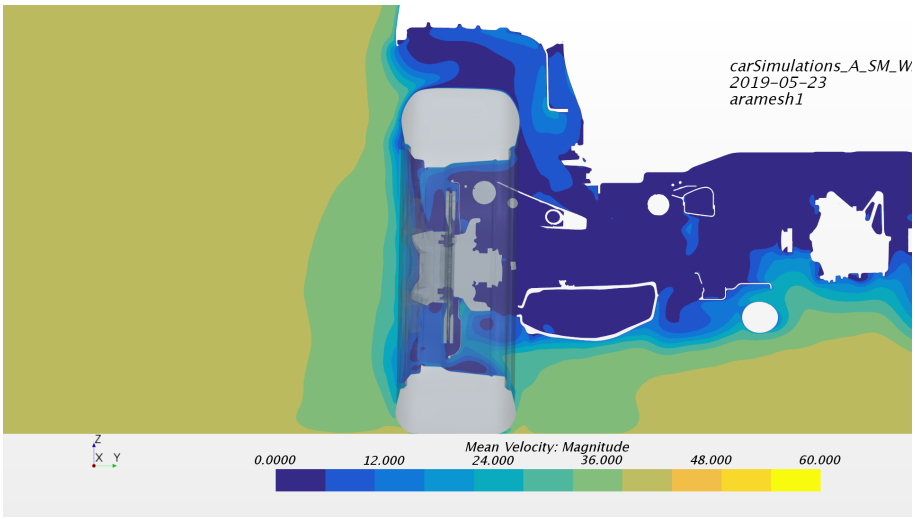

(b) Mean velocity field across the centre of the rear wheel

Figure 4.22: Mean velocity field across wheels on the left side of the car

As mentioned above, the flow in the wheel is extremely turbulent with the rotation of the wheels along with air entering and exiting the region. Fig. 4.22 represents a cross sectional plane about the front and the rear wheels on the left side of the car. It can be seen from Fig. 4.22a that the flow velocity magnitude around the front wheel is higher than the freestream velocity. This is because the flow accelerates around the front side bumpers and the front wheels as seen from the mean C_p plot in Fig. 4.19. The flow velocity reaches a higher value above the tyre bulge whereas on the upper part of the wheel, the velocity is very low at the region of the bulge.

The high velocity is because of the resultant of wheel rotation and on-coming flow while the low velocity is due to flow separation at the tyre bulge. In Fig. 4.22b, it can be seen that the flow is much slower near the rear wheel. The flow is slowed down by the combined effects of front wheel separation and skin friction drag on the fluid close to the body.
Flow separation can be visualized from the isosurface of mean $C_{p_{total}}$=0 colored by mean velocity field as seen in Fig. 4.23. It can seen from the figure that the front wheel consists of a bubble covered predominantly by high velocity region. The presence of this bubble indicates the separation of flow. The rear wheel, unlike the front, does not have a bubble covering the wheel and has lower velocity. Thus we can infer that the flow is relatively more attached.

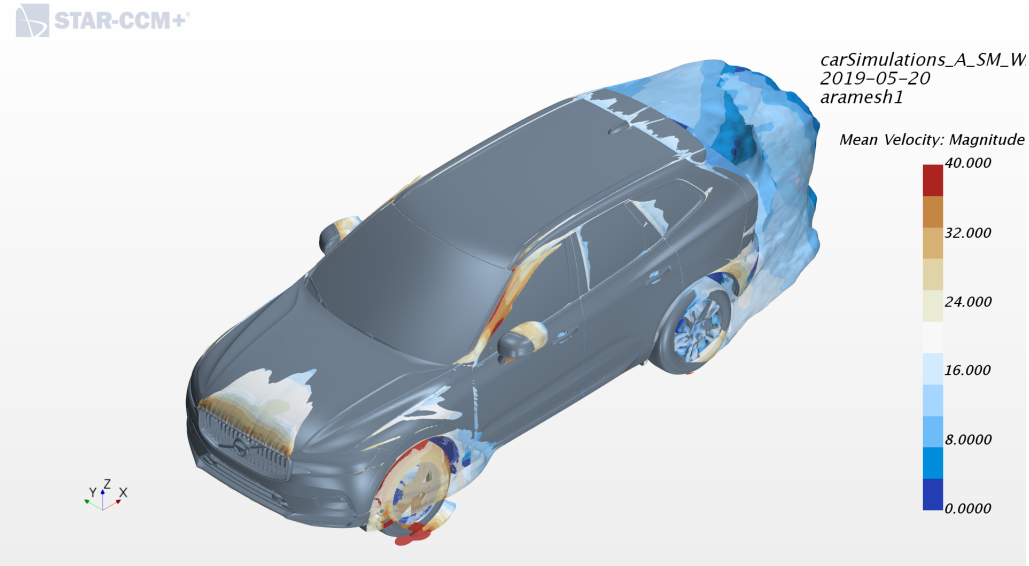

Figure 4.23: Mean $C_{p_{total}}$ on the surface of the car

The flow behind both the wheels is dominated by a wake after the flow passes around and over the tyres. Fig. 4.24 is the mean velocity field on a plane behind the wheel centres. It can be seen from Fig. 4.24a that the strength of the wake is stronger in the front wheel that then rear. This is because the flow has higher energy at the front wheels.

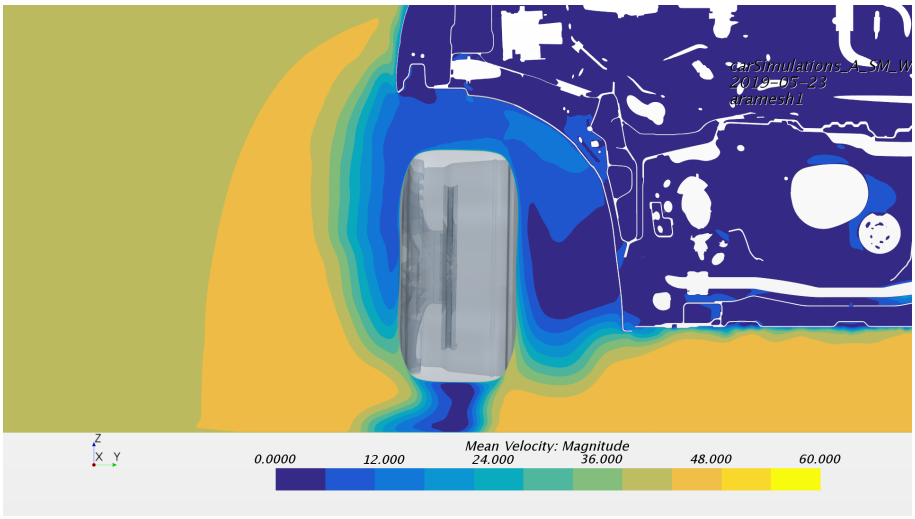

(a) Mean velocity field at 280mm behind the centre of the front wheel

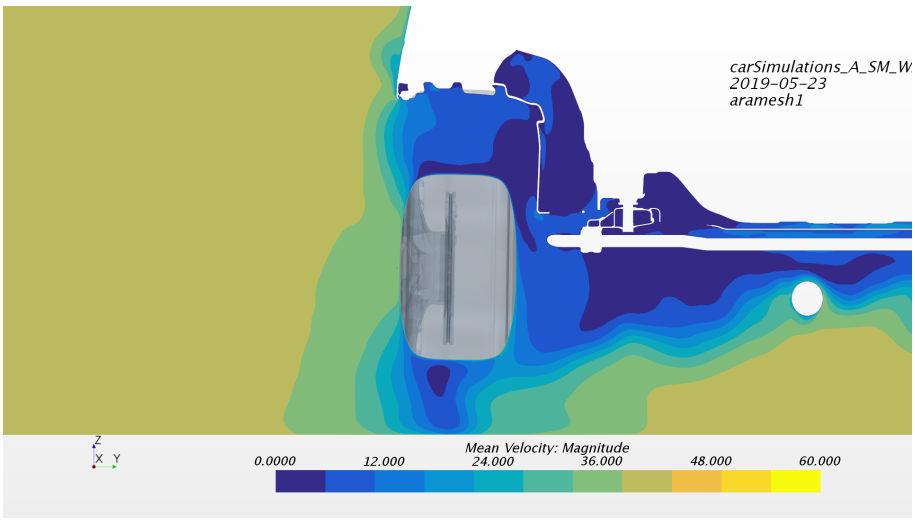

(b) Mean velocity field at 320mm behind the centre of the rear wheel

Figure 4.24: Mean velocity field behind the wheels to visualize the wake

4.2.3 Comparison between wheel modeling approaches-SM vs MRF

The non-dimensional aerodynamic variables are the key parameters to look for in a vehicle's performance. Table 4.6 compares the deltas of C_d, C_lr, C_lf and C_dA obtained from both the methods. Additionally, while comparing the two methods, the time taken for the simulation is also important because the SM approach has proved to be costly. It can be seen that the aerodynamic variables from both methods have very comparable values but the SM method takes about 6.3 hours more than MRF, which is about 25% more.

Quantity	Δ = MRF - SM
C_d	0.000
C_lr	0.004
C_lf	-0.001
C_dA	0.001
Time taken for simulation(hr)	-6.3

Table 4.6: Delta of various aerodynamic parameters of the car obtained from SM and MRF approaches

Fig. 4.25 represents the ΔC_dAx and ΔC_lAx plots obtained both the methods. The values are calculated by subtracting cumulative value at each local position of the car along x-axis. The profile obtained is due to the difference the flow field caused by the wheel modelling methodology. It can be seen that, the MRF method produces slightly higher drag and lift around the front wheel of the car. Along the body of the car, the difference in drag is almost constant whereas the MRF produces lower lift around the centre of the car. Near the rear wheel, the MRF method produces lower drag but higher lift as compared to SM method.

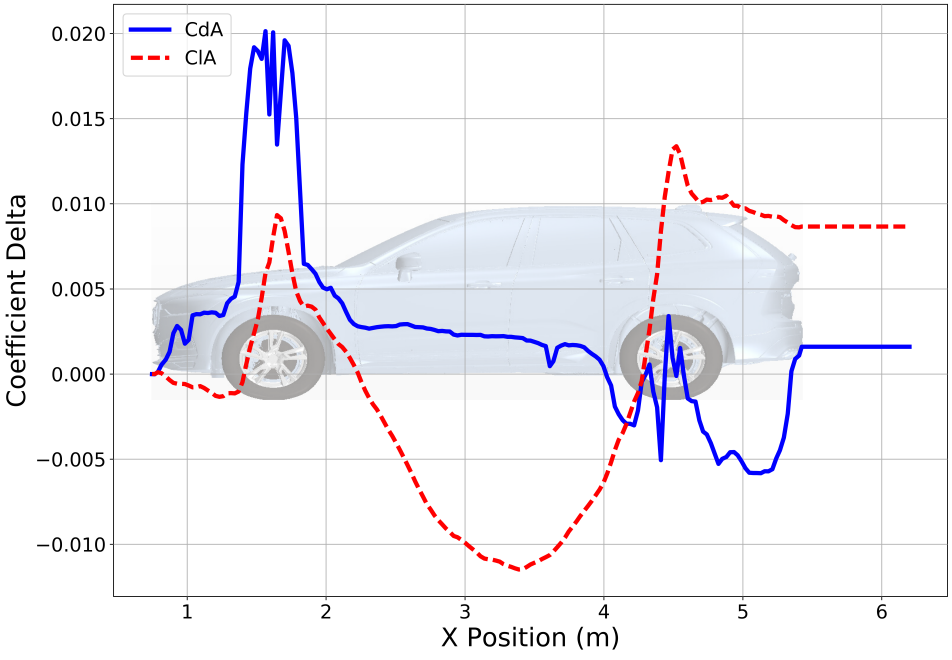

Figure 4.25: ΔC_dAx and ΔC_lAx plots for SM and MRF approaches

MRF is also called frozen rotor method as it accounts for rotation from a stationary framework. The position of the rim spokes can affect the mean flow field of the final solution as it remains stationary unlike SM where the mesh moves physically. The mean flow field in SM is completely averaged in the region of rotation. This makes

it difficult to consider the solution in the rotating region. Outside the sliding mesh region, the difference in wheel methodology causes a difference in the flow field. Fig. 4.26 represents the scalar cross section of the mean velocity field across the rear wheel from both the approaches. It can be seen that the flow over the rear brake discs and the rims is faster in the solution from MRF than in SM. The flow outside the wheel in MRF approach has a lower velocity along the rims as compared SM. The flow on the inner side of the wheel also follows a similar trend as seen in the figure.

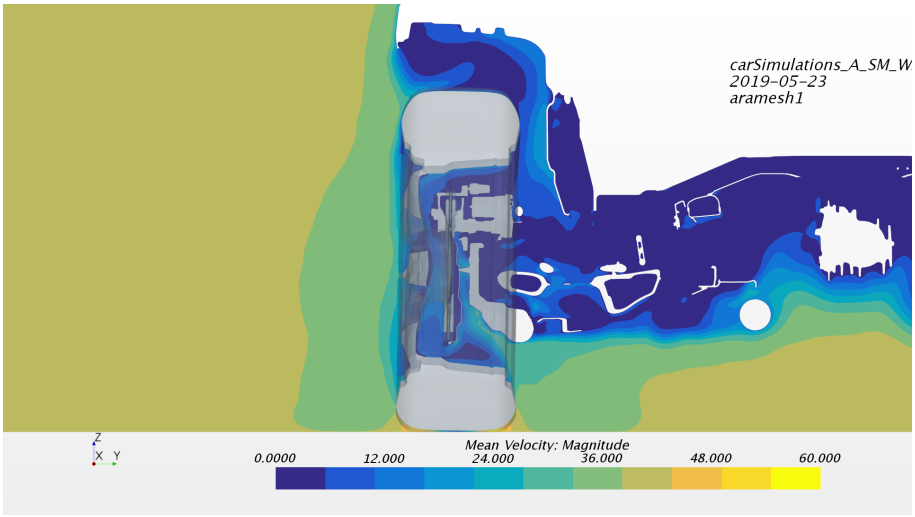

(a) Mean velocity field from SM approach

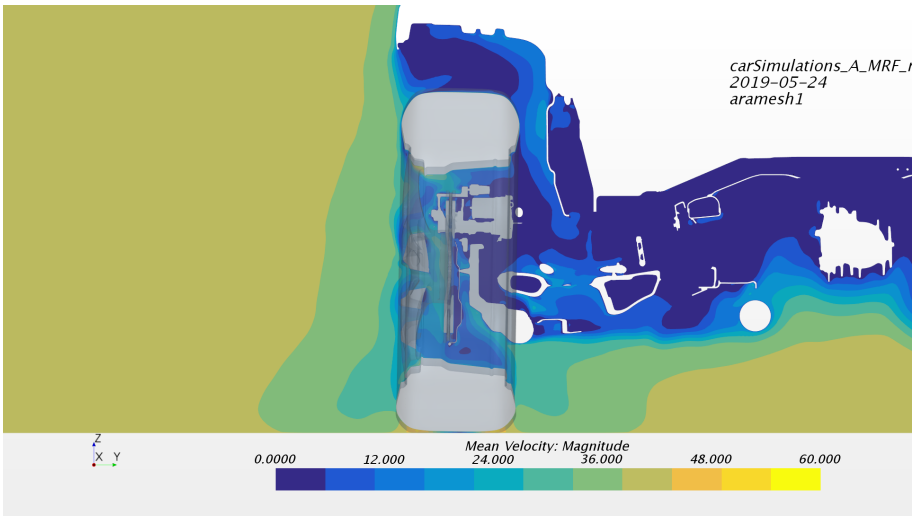

(b) Mean velocity field from MRF approach

Figure 4.26: Mean velocity field across the centre of the rear wheel of the car

In Fig. 4.25, the slope of the C_dA line increased sharply at the base of the car. So, the base pressure (Mean C_p) was compared between the two approaches as shown in

Fig. 4.27. It can be seen that the mean C_p values from the MRF solution in slightly lower than SM solution. This difference in the pressure could be the reason for steep slope in the $\Delta C_d Ax$ at the base. It can also be seen that, the C_p is asymmetric for the MRF solution as compared to SM solution. This is because of the underbody profile of the car. The SM simulation, due to mesh motion, is able to generate large disturbances in the flow near the wheels that reduces the asymmetric effect of the underbody profile. This effect is carried over almost equally on either sides of the base.

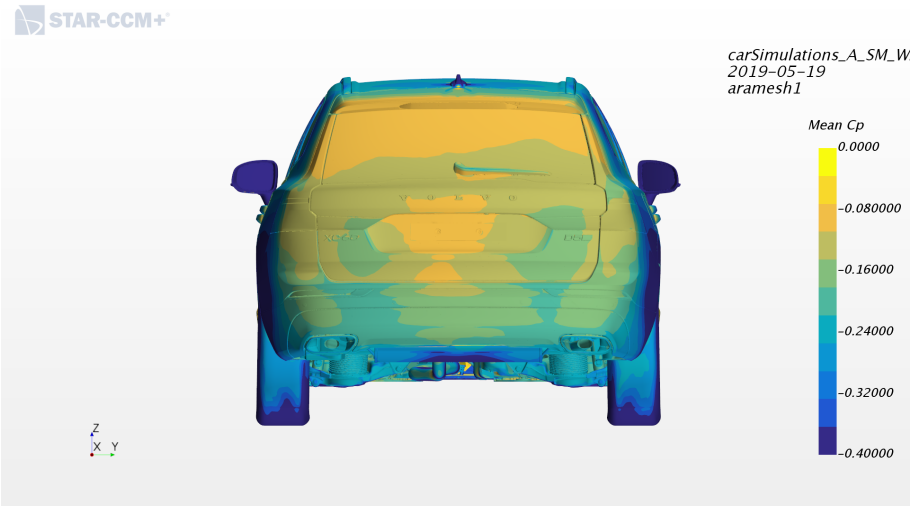

(a) Mean C_p from SM method

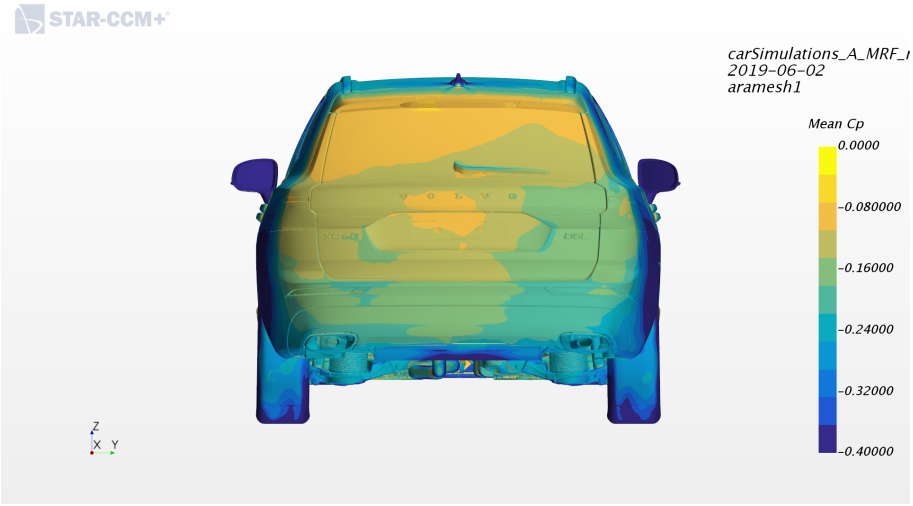

(b) Mean C_p from MRF method

Figure 4.27: Mean C_p on the base of the car comparing SM and MRF methods

4.2.4 Effect of rims in the flow field and aerodynamics of the car

As mentioned in section 3.2, two rims as shown in Fig. 3.11 were tested with the same conditions. Table 4.7 compares the deltas of aerodynamic variables from both the simulations.

Quantity	Δ = CR - OR
C_d	-0.011
$C_l r$	-0.008
$C_l f$	0.000
$C_d A$	-0.029

Table 4.7: *Delta* of various aerodynamic parameters comparing OR and CR

Fig. 4.28 represents the $\Delta C_d Ax$ and $\Delta C_l Ax$ of the car from either of the cases. The Δ is calculated as $C_{CR} - C_{OR}$. Blanking reduced 29 $C_d A$ counts and 21 $C_l A$ counts.

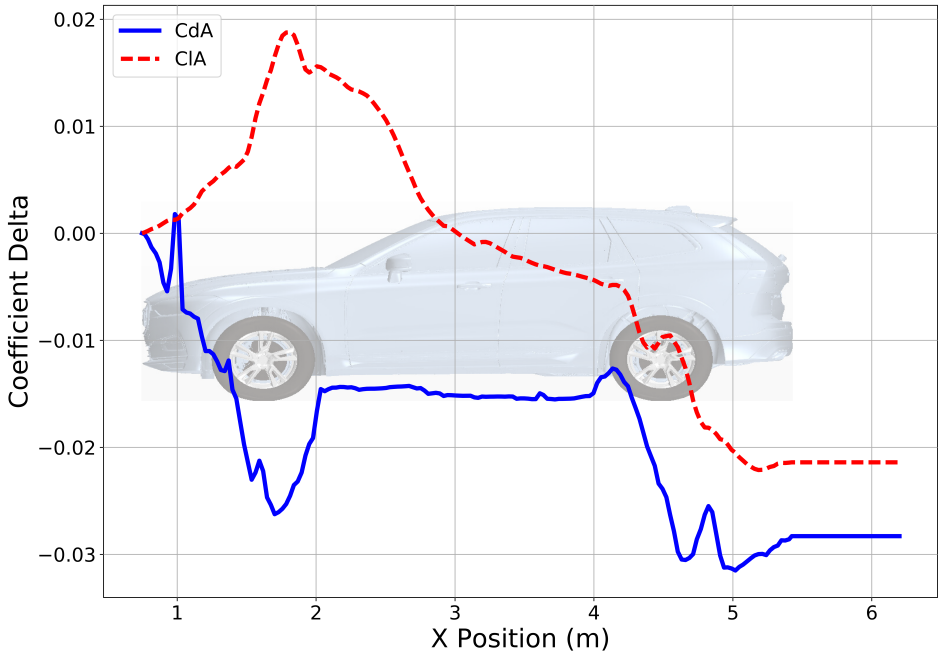

Figure 4.28: $\Delta C_d Ax$ and $\Delta C_l Ax$ plots for OR and CR

It is evident that closing the rim reduces the drag and increases the net downforce of the car. From Fig. 4.28, a small peak is observed near the front shutters. This is due to the difference in pressure caused between the two cases. CR has higher built in pressure with the rims closed. The effect of the rims carries forward to the front of the car resulting in lower drag. While the drag is reduced, the lift increases in the front of the car when the rims are closed. Along the rear wheels and wheel housing,

a significant reduction in the drag and lift is encountered. This is mainly because the flow is attached along the rims when they are closed and separation increases the drag significantly. However at the base of the car, it can be seen from Fig. 4.28 that CR produces slightly higher drag as compared to OR. This is because, OR produced higher base pressure as compared to CR. Higher base pressure results in lower drag.

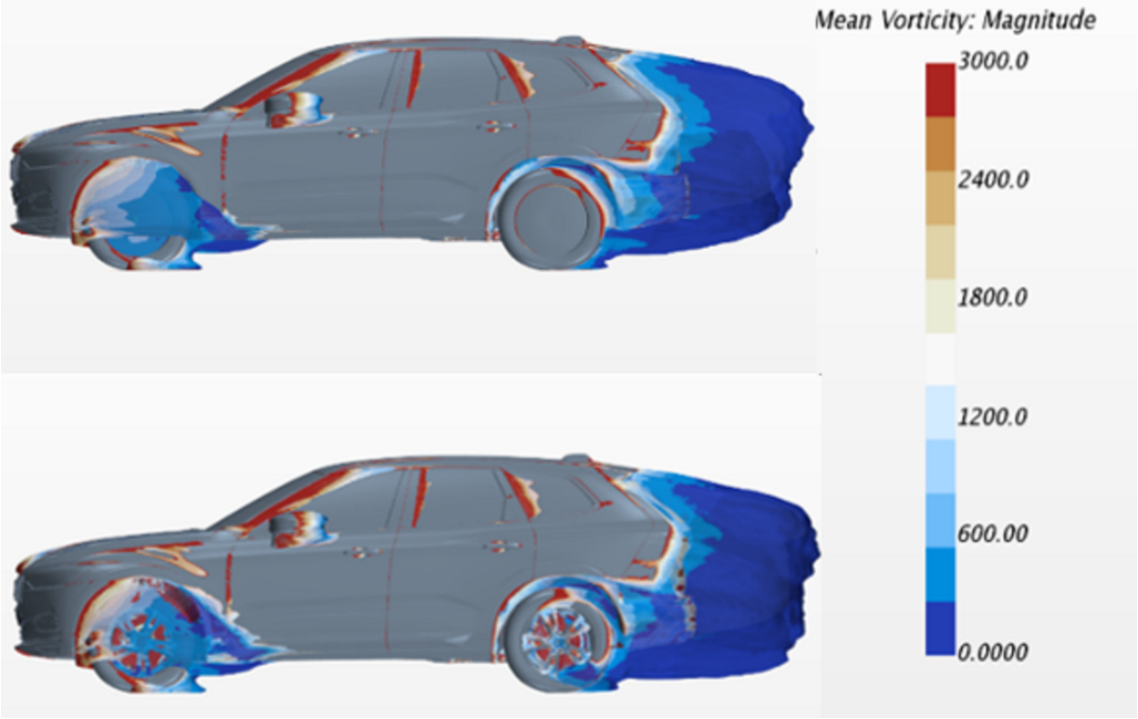

Figure 4.29: Iso-surface of mean $C_{p_{total}}$=0 coloured by mean vorticity comparing CR and OR

Fig. 4.29 represents an iso-surface of mean $C_{p_{total}} = 0$ coloured by mean vorticity in the flow comparing the solutions from OR and CR. Closing the rim prevents air flow in and out of the rim. This reduces the chaotic nature of flow around the wheels and tyres. Near the front wheel, blanking reduces the intensity of vorticity in the separation bubble slightly. The flow separates near the wheel housing lip and till the front door where it reattaches in either of the cases. But blanking the rim, reduces the intensity of the vortices generated. This preserves the mean fluid energy and helps in reducing the drag. The flow separation is not as prominent in the rear wheel as the velocity of the fluid is reduced. But closing the rims stopped separation along the rims. Though the flow still separated on the tyres, the flow was predominantly attached over the rims. The base wake observed was slightly shorter and thinner due to blanking.

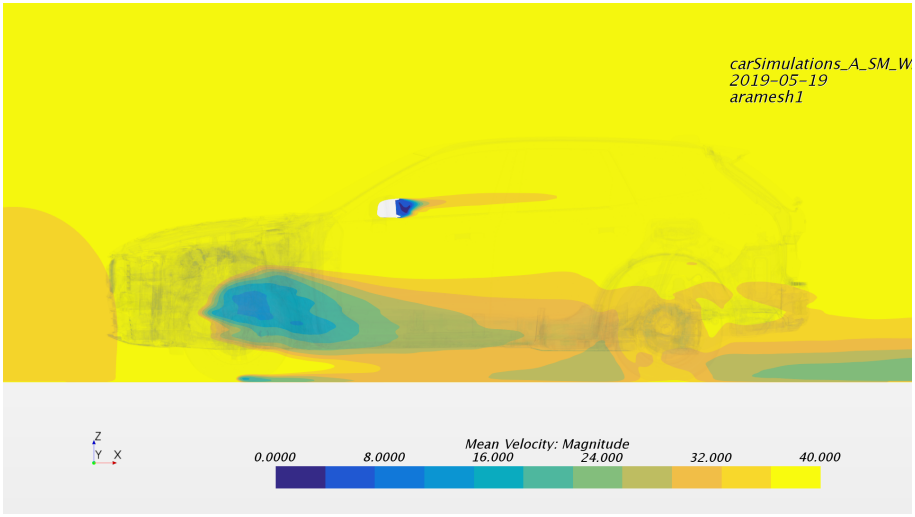

(a) Mean velocity field from OR

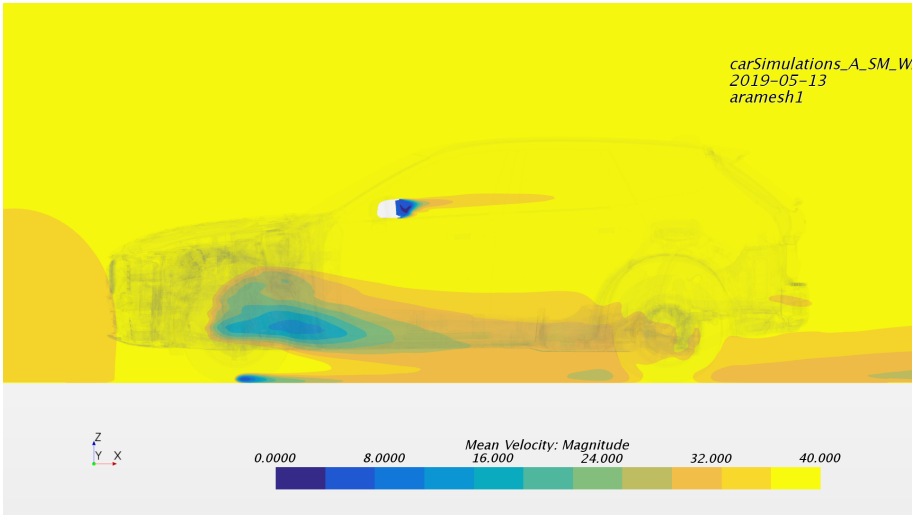

(b) Mean velocity field from CR

Figure 4.30: Mean velocity fields along a plane adjacent to the wheels

Fig. 4.30 represents the mean velocity of the flow field along a plane adjacent to the wheels. The influence of flow separation near wheels on the mean velocity field can be clearly visualized in this figure. The strength of the flow separation is stronger in OR. In the case of CR, the wakes are weaker and shorter. This allows higher energy flow to mix with the base wake. So we would naturally expect higher base pressure and upwash for CR. But we encountered lower base pressure for CR.

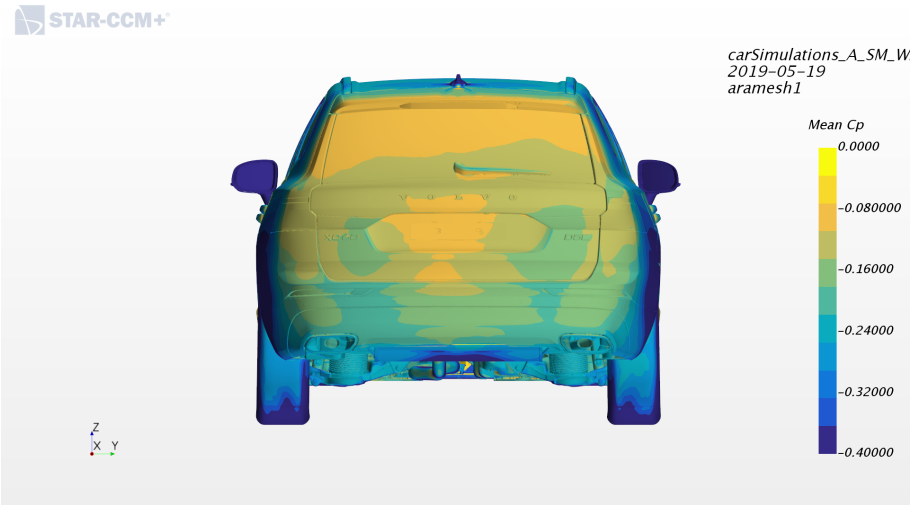

(a) Mean C_p field from OR

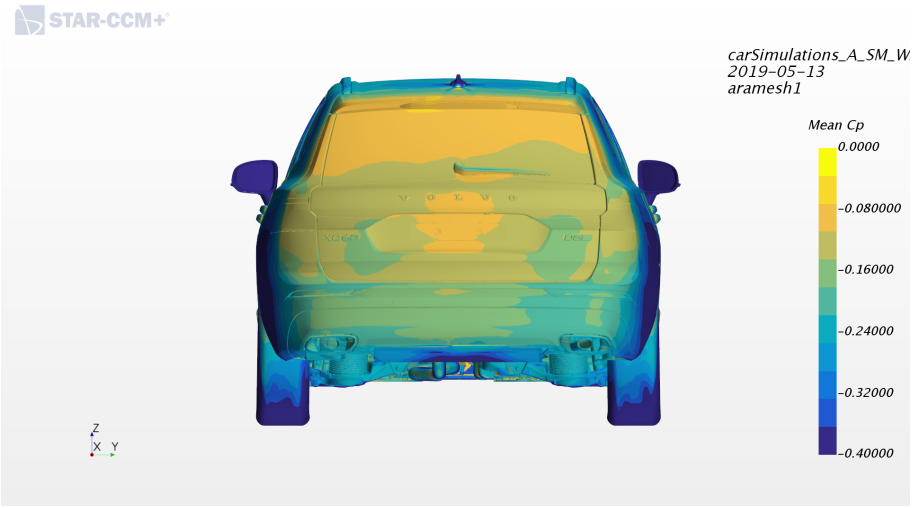

(b) Mean C_p field from CR

Figure 4.31: Mean C_p on the back of the car comparing OR and CR

Fig. 4.31 represents mean C_p on the rear end of the car. The pressure on the base is slightly different in these cases. In the CR case, the flow over the rim is more attached and faster as compared to OR as seen in Fig. 4.30. Though this allowed higher energy fluid to mix with the base wake which promotes higher base pressure, for this car, the mean C_p from the CR produced lower base pressure as seen in the figure. In comparison, OR produced slightly higher base pressure. That is why the drag increased at the base for CR in Fig. 4.28.
Fig. 4.32 represents mean velocity vector field at the base of the car. It can be seen that the flow field in the wake region is very similar from the two cases along the x-z plane. But the flow from CR produces slightly greater upwash and this is helped in obtaining greater downforce. This could be a reason for the slightly lower base

pressure for CR. The flow could have shifted to an angle which promotes greater upwash than base pressure.

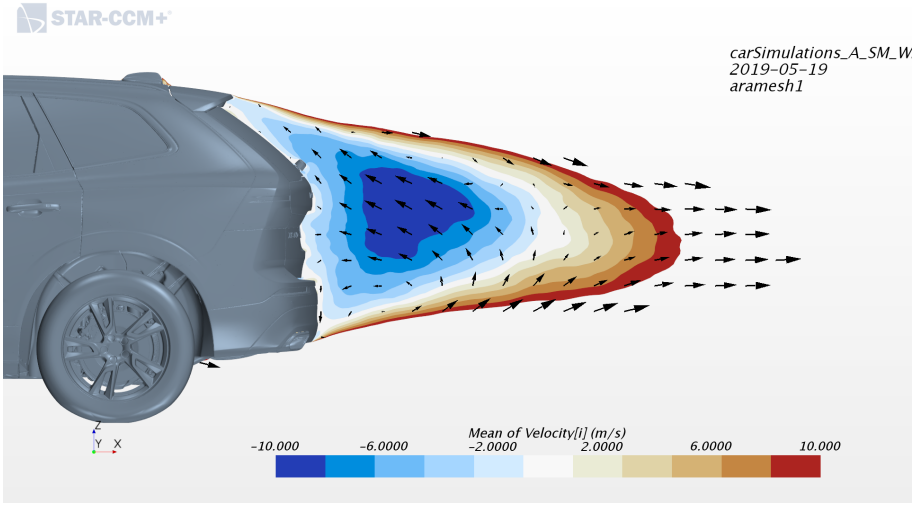

(a) Mean velocity vector field from OR

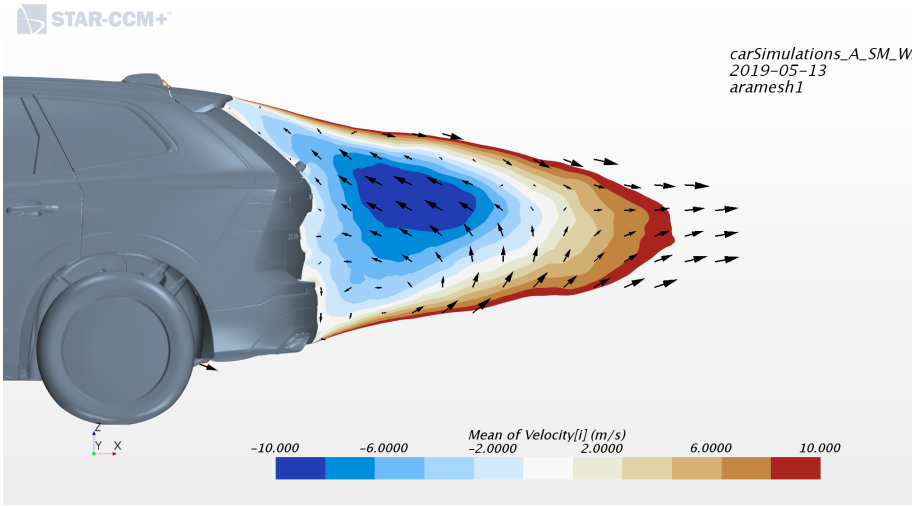

(b) Mean velocity vector field from CR

Figure 4.32: Mean velocity vector field on the back of the car comparing OR and CR

4.2.5 Time step dependency study

As stated in section 3.2, two time steps, 2.5e-4s and 1e-4s, were tested on the whole car setup. For consistency, the same mesh and run script was used and both were run on 2160 cores on the cluster. The table 4.8 consists of the Δ from both the simulations with the one with 2.5e-4 as the reference solution. The finer timestep of 1e-4s required much higher time. While the simulation with 2.5e-4s took 29 hours, the one with 1e-4s completed in 70 hours.

Quantity	Δ= $\mathbf{C}_{1e-4}$-$\mathbf{C}_{2.5e-4}$
C_d	0.001
C_lr	-0.002
C_lf	-0.003
C_dA	0.004

Table 4.8: Comparison of delta of mean values of aerodynamic variables for timestep dependency study

It can be seen that the simulation yielded only slightly different forces on the car. But given the time taken to achieve this solution, it can be inferred that the solution obtained with the timestep 2.5e-4s is acceptable. The Fig. 4.33 shows the ΔC_dAx and ΔC_lAx of both cases.

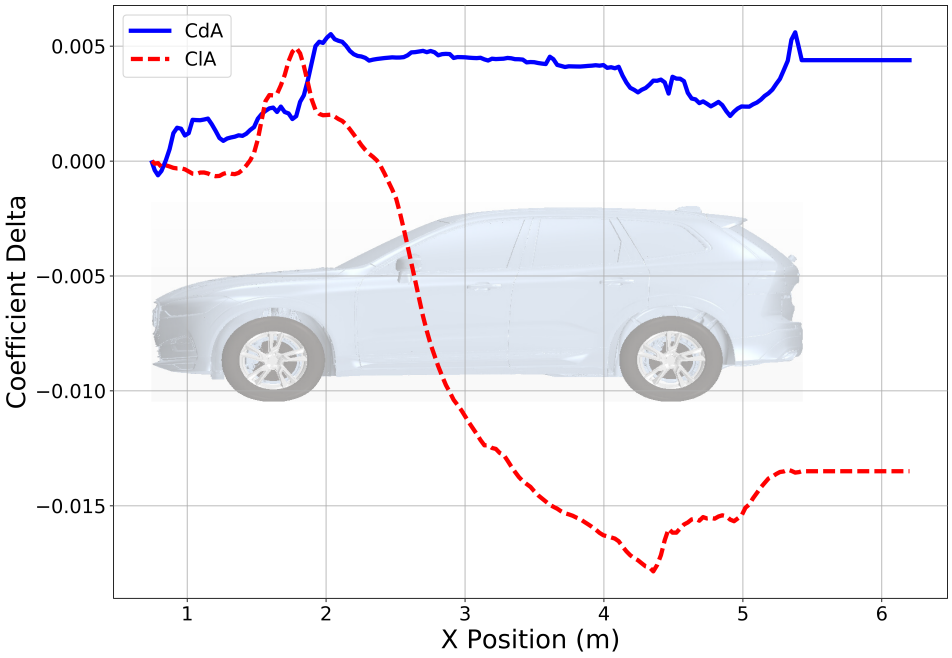

Figure 4.33: ΔC_dAx and ΔC_lAx plots timestep dependency study

In terms of the stability of the solution, both the cases performed well. The residuals and the aerodynamic variables converged to similar solutions and were quite stable.

Preserving the mesh and changing the timestep results in a different Courant number in the domain. Fig. 4.34 compares solution for a CFL number greater than 1. It can be seen that the solution with the coarser time step has a greater region with CFL>1. But the majority of it still under a reasonably accepted level(<5). A second order spatial discretization scheme is used in the two cases. Additionally, the solution is obtained using a implicit solver, iterated many times per timestep. Hence for a converged simulation, the final solution should not vary much and that is evident from the table. 4.8. Hence, it is sufficient to run the simulation with 2.5e-4s.

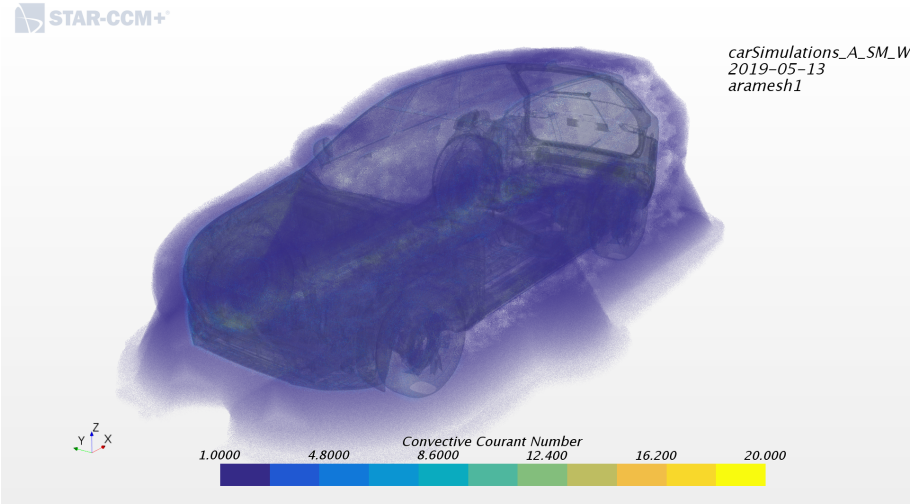

(a) CFL number for time step 2.5e-4s

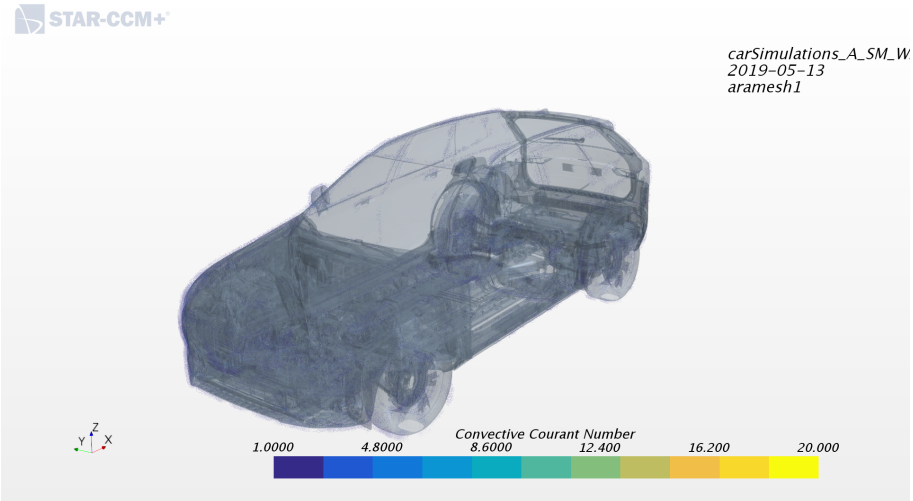

(b) CFL number for time step 1e-4s

Figure 4.34: CFL number comparison between both the cases

4.2.6 Splitting interface - Pseudo-parallelization

The results from the cylinder simulations were promising and the methodology was adopted for modelling wheels as shown in Fig. 3.12. The method required the user to split the interface in such as way that the number of faces from the rotating and stationary regions, intersecting the interface are equal. But due to the complexity of the rims intersecting the domain, this was difficult to achieve. The final setup had a split ratio of 2:2:1 intersecting faces across the three interfaces. Table. 4.9 presents the time per timestep, time per iteration and the time taken for updating the mesh per timestep.

Quantity	**1 interface**	**3 interfaces**
Time per timestep(s)	11.1	10.5
Time per iteration(s)	1.32	1.33
Time for updating(s)	3.18	2.52

Table 4.9: Results from interface splitting

The interface for each wheel consisted of 200,000 cells intersecting from both the stationary and rotating regions. The Fig. 4.35 represents the split of intersecting cells across the three interfaces. This uneven distribution resulted in unequal CPU load and the approach does not run at optimal capacity.

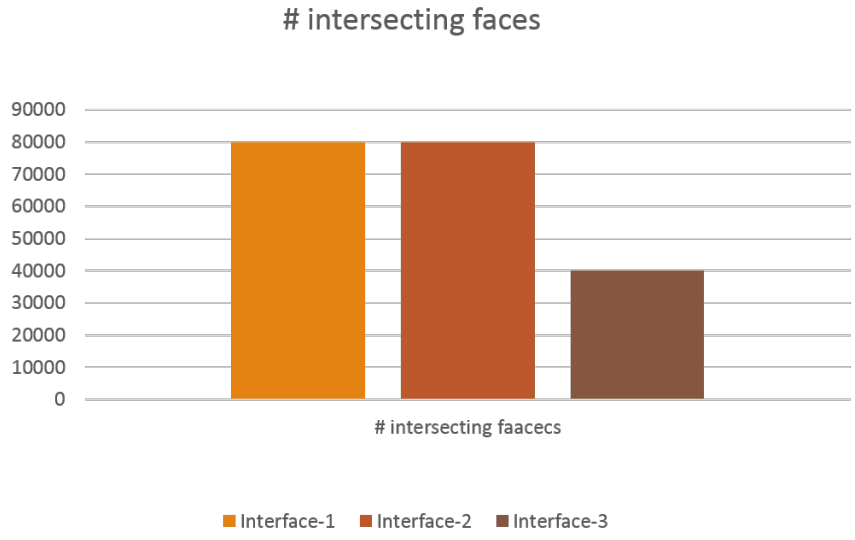

Figure 4.35: Comparison of the number of intersecting cells across the three interfaces

It can seen from the table that, this method decreased the time taken for updating the mesh and interface each timestep. About 20.7% reduction in the time for updating, 5% reduction in time per timestep and 1% increase in time per iteration were noted. The cylinder simulations recorded over 50% reduction in the updating time and 30% reduction in time per timestep. The simulation on the car is extremely big as compared to the cylinder and proportional results can not be expected. The

cylinder had about 96,000 intersection faces along the interface while each wheel had 200,000 intersecting faces and the number of faces on the each of the interface of the wheel were not split evenly. But by splitting the number of faces evenly on all the three interfaces, the updating time could be further improved. Like in the results from the cylinder, the simulation on the car also exhibited increase in time per iteration with higher number of interfaces. While there was a 2% increase in iteration time for the cylinder, there was 1% increase in the car. Like in the cylinder case, this is because the solution updating at the beginning of each timestep across the interface takes more time when boundary mode interfaces are created. So, the first iteration takes slightly more time than the rest which increases the mean iteration time. Additionally, increasing the number of boundaries increases the iteration time.
Table 4.10 presents the Δ of the aerodynamic variables from either of the solutions. The change in setup did not alter the final solution by much. So boundary mode interfacing does not change the solution.

Quantity	$\Delta = \mathbf{C}_{3int}$**-** $\mathbf{C}_{1int}$
C_d	0.001
$C_l r$	-0.005
$C_l f$	0.000
$C_d A$	0.004

Table 4.10: Comparison of delta of aerodynamic variables for pseudo-parallelization study

It can be inferred that this method is viable for speeding up the simulation. Splitting the surface into more than 3 PIDs is also an option to further improve the speedup. But it essential to be cautious on the time spent in doing this. This process of creating multiple PIDs is a manual process done on ANSA which is time consuming. Additionally, with growing number of interfaces, the time per iteration also increases. So it is necessary to be aware that the effective time spent on the simulation could increase if too much time is spent on the setup creating many surfaces for the wheel which results in spending more time per iteration. So, the method has to be optimized for each application.

5
Conclusion

The thesis presents a number of CFD studies, investigating a simple rotating cylinder and then a car.

Analysis on rotation modelling was performed on a rotating cylinder comparing RW and SM methods. A mesh, timestep and solver sensitivity study was performed on SM method. Pseudo-parallelization approach for SM was tested and analyzed on the cylinder.

After studying the flow field around the car, MRF and SM wheel modelling approaches were analyzed. The effects of blanking on the aerodynamic performance of the car was studied. A timestep sensitivity study was performed. Finally, pseudo-parallelization approach for SM was tested on the car.

The main outcomes from the work are presented below:
Cylinder simulations

- Both RW and SM methods produced very similar results when an adequate mesh size and timestep were used.
- The SM method was more sensitive to mesh size and timestep selection than RW. From the parametric study, a coarser configuration was suggested for SM to obtain comparable results to RW at low simulation cost.
- Pseudo-parallelization approach yielded 68% reduction in mesh updating time and 9% increase in iteration time when 8 interfaces was used. This resulted in 35% reduction in total time. It was inferred that this approach could be used for speeding up SM simulations.

Car Simulations

- MRF and SM methods produced similar values for the aerodynamic variables. But the flow field locally around the wheels and the base of the car was quite different.
- Since SM method is more realistic in the modelling approach, it is recommended for the modelling of rims.
- Blanking the rims reduced the drag by 29 C_dA counts and lift by 21 C_lA counts for this car. This reduction in drag was due to lower flow separation for CR around the wheels as compared to OR. This allowed high energy fluid to mix with the base wake which increased the upwash, producing higher downforce.
- From the timestep dependency study, it was found that for the current mesh settings, a timestep of 2.5e-4s is capable of producing acceptable results.

- Pseudo-parallelization approach on SM for the car produced about 21% reduction in mesh updating time when three interfaces were used. The number of intersecting faces across the interface was not evenly split across them. So by splitting the intersecting faces evenly across the interface and creating more than three interfaces, this method can be further improved.

5.1 Future Work

A few suggestions for future work are listed below:

- Experimental investigations to validate the solution obtained from the simulations on the rotating cylinder could be useful to further investigate the accuracy of rotation modelling techniques in CFD.
- Pseudo-parallelization method has a lot of potential for speeding up SM simulations and this can be investigated more.
- Investigate mesh resolution sensitivity with a especially attention to the interfaces.
- Modelling contact patch.
- FEM-CFD coupling to model the contact patch to obtain the exact solution for wheel modelling.

Bibliography

[1] Hobeika, T., 2018. Wheel Modelling and Cooling Flow Effects on Car Aerodynamics. Chalmers University of Technology.

[2] Landstrom, C., Josefsson, L., Walker, T. and Lofdahl, L., 2012. Aerodynamic effects of different tire models on a sedan type passenger car. SAE International Journal of Passenger Cars-Mechanical Systems, 5(2012-01-0169), pp.136-151.

[3] Wittmeier, F. and Kuthada, T., 2015. The influence of wheel and tire aerodynamics in WLTP. In 6th International Munich Chassis Symposium 2015 (pp. 149-160). Springer Vieweg, Wiesbaden.

[4] Ten Brink, P., 2010. Mitigating CO2 emissions from cars in the EU (Regulation (EC) No. 443/2009). The new climate policies of the European Union: Internal legislation and climate diplomacy, 15, p.179.

[5] European Parliament and the Council of the European Union, 2014. Regulation (EU) No 333/2014 of the European Parliament and of the Council of 11 March 2014 amending Regulation (EC) No 443/2009 to define the modalities for reaching the 2020 target to reduce CO2 emissions from new passenger cars. Off J Eur Union, 103(333), pp.15-21.

[6] Kandasamy, S., Duncan, B., Gau, H., Maroy, F., Belanger, A., Gruen, N. and Schäufele, S., 2012. Aerodynamic performance assessment of BMW validation models using computational fluid dynamics (No. 2012-01-0297). SAE Technical Paper.

[7] Fackrell, J.E. and Harvey, J.K., 1972. The flow field and pressure distribution of an isolated road wheel.

[8] Cogotti,A., "Aerodynamics Characteristics of Car Wheels", 1983, International Journal of Vehicle Design, SP3.

[9] Mercker, E., Berneburg, H., 1992," On the simulation of Road Driving of a Passenger Car in a Windtunnel Using a Moving Belt and Rotating Wheels", Lecture at the Third International Conference Innovation and Reliability in Automotive Design and Testing, Florence.

[10] Elofsson, P. and Bannister, M., 2002. Drag reduction mechanisms due to moving ground and wheel rotation in passenger cars. SAE Transactions, pp.591-604.

[11] Landström, C., Walker, T., Christoffersen, L. and Löfdahl, L., 2011. Influences of different front and rear wheel designs on aerodynamic drag of a sedan type passenger car (No. 2011-01-0165). SAE Technical Paper.

[12] Zhiling, Q., Landström, C., Löfdahl, L. and Josefsson, L., 2010. Wheel Aerodynamic Developments on Passenger Cars by Module-based Prototype Rims and Stationary Rim Shields. In FISITA 2010 Automotive World Congress.

[13] Hobeika, T., Sebben, S. and Landstrom, C., 2013. Investigation of the influence of tyre geometry on the aerodynamics of passenger cars. SAE International Journal of Passenger Cars-Mechanical Systems, 6(2013-01-0955), pp.316-325.

[14] Hobeika, T. and Sebben, S., 2018. CFD investigation on wheel rotation modelling. Journal of Wind Engineering and Industrial Aerodynamics, 174, pp.241-251.

[15] Koitrand, S., Gaylard, A. and Fiet, G.O., 2015. 18 An Investigation of Wheel Aerodynamic Effects for a Saloon Car.

[16] Blacha, T. and Islam, M., 2017. The aerodynamic development of the new Audi Q5. SAE International Journal of Passenger Cars-Mechanical Systems, 10(2017-01-1522), pp.638-648.

[17] Schnepf, B., Schütz, T. and Indinger, T., 2015. Further investigations on the flow around a rotating, isolated wheel with detailed tread pattern. SAE International Journal of Passenger Cars-Mechanical Systems, 8(2015-01-1554), pp.261-274.

[18] Profir, M.M., 2012. Automated moving mesh techniques and re-meshing strategies in CFD applications using morphing and rigid motions.

[19] SIEMENS, P. L. M. STAR-CCM+ Documentation. 2018, Siemens PLM Software Inc, 13.

[20] Axon, L., Garry, K. and Howell, J., 1998. An evaluation of CFD for modelling the flow around stationary and rotating isolated wheels. SAE transactions, pp.205-215.

[21] Gritskevich, M.S., Garbaruk, A.V., Schütze, J. and Menter, F.R., 2012. Development of DDES and IDDES formulations for the k- shear stress transport model. Flow, turbulence and combustion, 88(3), pp.431-449.

[22] Davidson, Lars. 2018. *Fluid mechanics, turbulent flow and turbulence modeling*. Göteborg: Division of fluid mechanics, Department of Applied Mechanics, Chalmers University of Technology. URL: `http://www.tfd.chalmers.se/~lada/postscript_files/solids-and-fluids_turbulent-flow_turbulence-modelling.pdf`

[23] Davidson, L., 2015. An introduction to turbulence models.

[24] Roshko, A. (1961). Experiments on the flow past a circular cylinder at very high Reynolds number. Journal of Fluid Mechanics, 10(3), 345-356.